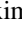







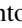





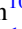




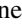

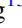








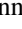
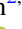


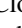
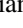




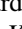
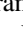

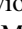


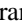


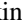





Unveiling the Distant Universe: Characterizing $z \geq 9$ Galaxies in the First Epoch of COSMOS-Web

Maximilien Franco¹ , Hollis B. Akins¹ , Caitlin M. Casey¹ , Steven L. Finkelstein¹ , Marko Shuntov² , Katherine Chworowsky¹ , Andreas L. Faisst³ , Seiji Fujimoto^{1,41} , Olivier Ilbert⁴ , Anton M. Koekemoer⁵ , Daizhong Liu⁶ , Christopher C. Lovell^{7,8} , Claudia Maraston⁹ , Henry Joy McCracken¹⁰ , Jed McKinney¹ , Brant E. Robertson¹¹ , Micaela B. Bagley¹ , Jaclyn B. Champagne¹² , Olivia R. Cooper^{1,42} , Xuheng Ding¹³ , Nicole E. Drakos¹¹ , Andrea Enia^{14,15} , Steven Gillman^{2,16} , Ghassem Gozaliasl^{17,18} , Santosh Harish¹⁹ , Christopher C. Hayward²⁰ , Michaela Hirschmann^{21,22} , Shuowen Jin^{2,16,24} , Jeyhan S. Kartaltepe¹⁹ , Vasily Kokorev²³ , Clotilde Laigle¹⁰ , Arianna S. Long^{1,41} , Georgios Magdis^{2,16,24} , Guillaume Mahler^{25,26} , Crystal L. Martin²⁷ , Richard Massey^{25,26} , Bahram Mobasher²⁸ , Louise Paquereau¹⁰ , Alvio Renzini²⁹ , Jason Rhodes³⁰ , R. Michael Rich³¹ , Kartik Sheth³² , John D. Silverman^{33,34,35} , Martin Sparre³⁶ , Margherita Talia^{14,37} , Benny Trakhtenbrot³⁸ , Francesco Valentino^{2,24} , Aswin P. Vijayan^{2,16} , Stephen M. Wilkins^{8,39} , Lilan Yang¹³ , and Jorge A. Zavala⁴⁰ 

¹ The University of Texas at Austin, 2515 Speedway Blvd. Stop C1400, Austin, TX 78712, USA; maximilien.franco@austin.utexas.edu

² Cosmic Dawn Center (DAWN), Denmark

³ Caltech/IPAC, 1200 E. California Blvd., Pasadena, CA 91125, USA

⁴ Aix Marseille Université, CNRS, CNES, LAM, Marseille, France

⁵ Space Telescope Science Institute, 3700 San Martin Dr., Baltimore, MD 21218, USA

⁶ Max-Planck-Institut für Extraterrestrische Physik (MPE), Giessenbachstr. 1, D-85748 Garching, Germany

⁷ Institute of Cosmology and Gravitation, University of Portsmouth, Burnaby Rd., Portsmouth, PO1 3FX, UK

⁸ Astronomy Centre, University of Sussex, Falmer, Brighton, BN1 9QH, UK

⁹ Institute of Cosmology and Gravitation, University of Portsmouth, Dennis Sciama Building, Burnaby Road, Portsmouth, PO1 3FX, UK

¹⁰ Institut d'Astrophysique de Paris, UMR 7095, CNRS, and Sorbonne Université, 98 bis boulevard Arago, F-75014 Paris, France

¹¹ Department of Astronomy and Astrophysics, University of California, Santa Cruz, 1156 High St., Santa Cruz, CA 95064, USA

¹² Steward Observatory, University of Arizona, 933 N Cherry Ave., Tucson, AZ 85721, USA

¹³ Kavli Institute for the Physics and Mathematics of the Universe (WPI), The University of Tokyo, Kashiwa, Chiba 277-8583, Japan

¹⁴ University of Bologna—Department of Physics and Astronomy “Augusto Righi” (DIFA), Via Gobetti 93/2, I-40129, Bologna, Italy

¹⁵ INAF—Osservatorio di Astrofisica e Scienza dello Spazio, Via Gobetti 93/3, I-40129, Bologna, Italy

¹⁶ DTU-Space, Technical University of Denmark, Elektrovej 327, DK-2800 Kgs. Lyngby, Denmark

¹⁷ Department of Computer Science, Aalto University, PO Box 15400, Espoo, FI-00076, Finland

¹⁸ Department of Physics, University of Helsinki, P.O. Box 64, FI-00014 Helsinki, Finland

¹⁹ Laboratory for Multiwavelength Astrophysics, School of Physics and Astronomy, Rochester Institute of Technology, 84 Lomb Memorial Dr., Rochester, NY 14623, USA

²⁰ Center for Computational Astrophysics, Flatiron Institute, 162 Fifth Ave., New York, NY 10010, USA

²¹ Institute of Physics, GalSpec, École Polytechnique Fédérale de Lausanne, Observatoire de Sauverny, Chemin Pegasi 51, 1290 Versoix, Switzerland

²² INAF, Astronomical Observatory of Trieste, Via Tiepolo 11, 34131 Trieste, Italy

²³ Kapteyn Astronomical Institute, University of Groningen, PO Box 800, 9700 AV Groningen, The Netherlands

²⁴ Niels Bohr Institute, University of Copenhagen, Jagtvej 128, DK-2200, Copenhagen, Denmark

²⁵ Department of Physics, Centre for Extragalactic Astronomy, Durham University, South Road, Durham, DH1 3LE, UK

²⁶ Department of Physics, Institute for Computational Cosmology, Durham University, South Road, Durham, DH1 3LE, UK

²⁷ Department of Physics, University of California, Santa Barbara, Santa Barbara, CA 93109, USA

²⁸ Department of Physics and Astronomy, University of California, Riverside, 900 University Ave., Riverside, CA 92521, USA

²⁹ INAF, Osservatorio Astronomico di Padova, Vicolo dell'Osservatorio 5, I-35122 Padova, Italy

³⁰ Jet Propulsion Laboratory, California Institute of Technology, 4800 Oak Grove Dr., Pasadena, CA 91001, USA

³¹ Department of Physics and Astronomy, UCLA, PAB 430 Portola Plaza, Box 951547, Los Angeles, CA 90095-1547, USA

³² NASA Headquarters, 300 Hidden Figures Wy. SE, Washington, DC 20546, USA

³³ Kavli Institute for the Physics and Mathematics of the Universe (Kavli IPMU, WPI), UTIAS, Tokyo Institutes for Advanced Study, University of Tokyo, Chiba, 277-8583, Japan

³⁴ Department of Astronomy, School of Science, The University of Tokyo, 7-3-1 Hongo, Bunkyo, Tokyo 113-0033, Japan

³⁵ Center for Data-Driven Discovery, Kavli IPMU (WPI), UTIAS, The University of Tokyo, Kashiwa, Chiba 277-8583, Japan

³⁶ Institut für Physik und Astronomie, Universität Potsdam, Karl-Liebknecht-Str. 24/25, 14476 Golm, Germany

³⁷ INAF, Osservatorio di Astrofisica e Scienza dello Spazio, Via Gobetti 93/3, I-40129, Bologna, Italy

³⁸ School of Physics and Astronomy, Tel Aviv University, Tel Aviv 69978, Israel

³⁹ Institute of Space Sciences and Astronomy, University of Malta, Msida, MSD 2080, Malta

⁴⁰ National Astronomical Observatory of Japan, 2-21-1 Osawa, Mitaka, Tokyo 181-8588, Japan

Received 2023 August 1; revised 2024 June 10; accepted 2024 July 1; published 2024 September 12



Original content from this work may be used under the terms of the [Creative Commons Attribution 4.0 licence](https://creativecommons.org/licenses/by/4.0/). Any further distribution of this work must maintain attribution to the author(s) and the title of the work, journal citation and DOI.

⁴¹ NASA Hubble Fellow.

⁴² NSF Graduate Research Fellow.

Abstract

We report the identification of 15 galaxy candidates at $z \geq 9$ using the initial COSMOS-Web JWST observations over 77 arcmin^2 through four Near Infrared Camera filters (F115W, F150W, F277W, and F444W) with an overlap with the Mid-Infrared Imager (F770W) of 8.7 arcmin^2 . We fit the sample using several publicly available spectral energy distribution (SED) fitting and photometric redshift codes and determine their redshifts between $z = 9.3$ and $z = 10.9$ ($\langle z \rangle = 10.0$), UV magnitudes between $M_{\text{UV}} = -21.2$ and -19.5 (with $\langle M_{\text{UV}} \rangle = -20.2$), and rest-frame UV slopes ($\langle \beta \rangle = -2.4$). These galaxies are, on average, more luminous than most $z \geq 9$ candidates discovered by JWST so far in the literature, while exhibiting similar blue colors in their rest-frame UV. The rest-frame UV slopes derived from SED fitting are blue ($\beta \sim [-2.0, -2.7]$) without reaching extremely blue values as reported in other recent studies at these redshifts. The blue color is consistent with models that suggest the underlying stellar population is not yet fully enriched in metals like similarly luminous galaxies in the lower-redshift Universe. The derived stellar masses with $(\log_{10}(M_*/M_\odot)) \approx 8\text{--}9$ are not in tension with the standard Lambda cold dark matter (Λ CDM) model, and our measurement of the volume density of such UV-luminous galaxies aligns well with previously measured values presented in the literature at $z \sim 9\text{--}10$. Our sample of galaxies, although compact, is significantly resolved.

Unified Astronomy Thesaurus concepts: [Early universe \(435\)](#); [Galaxy evolution \(594\)](#); [High-redshift galaxies \(734\)](#); [Galaxy formation \(595\)](#)

1. Introduction

The search for and characterization of the most distant galaxies in the Universe is fundamental to our understanding of galaxy formation and evolution as a whole. However, we know very little about the first galaxies at $z > 10$. Prior to JWST, only one galaxy was confirmed at these redshifts (GN-z11; Oesch et al. 2016; Bunker et al. 2023). The recent launch of JWST, with its unprecedented angular resolution and sensitivity at IR wavelengths, is now providing the ideal observations to study star formation in high-redshift galaxies at rest-frame optical wavelengths. As a result, the number of $z \geq 9$ candidates has increased significantly (e.g., Pontoppidan et al. 2022; Castellano et al. 2022; Naidu et al. 2022; Whitler et al. 2023; Finkelstein et al. 2022; Adams et al. 2023; Austin et al. 2023; Leung et al. 2023; Casey et al. 2024) with some spectroscopically confirmed systems reaching up to $z \sim 13$ (Robertson et al. 2023; Curtis-Lake et al. 2023) and candidates up to $z \sim 17$ (Harikane et al. 2022; Atek et al. 2023a; Finkelstein et al. 2023; Austin et al. 2023; Hainline et al. 2024).

Extragalactic JWST surveys that aim for the high-redshift Universe have adopted various complementary strategies, including some very deep surveys, e.g., NGDEEP (GO #2079); others combining advantageously the observations of several JWST instruments, e.g., JADES (GTO #1180, 1210, and 1287; Eisenstein et al. 2023) and CEERS (ERS #1345; Finkelstein et al. 2023); or observing strongly lensed fields, e.g., UNCOVER (GO #2561; Bezanson et al. 2022) and GLASS-JWST-ERS (GO #1324; Treu et al. 2022). The unique strength of the COSMOS-Web program (GO #1727; Casey et al. 2023) is its large area, 3 times larger than all other JWST deep-field programs combined. When complete, in 2024 January, COSMOS-Web will cover a contiguous 0.54 deg^2 with the Near Infrared Camera (NIRCam; Rieke et al. 2003, 2005, 2023; Beichman et al. 2012). This wide area opens up a specific parameter space during the Epoch of Reionization (EoR), which remains inaccessible with other smaller surveys of particularly intrinsically bright galaxies ($M_{\text{UV}} < -20$; Finkelstein et al. 2023) while effectively reducing uncertainties in fundamental extragalactic measurements resulting from cosmic variance (at $z \sim 9$ the cosmic variance, σ_v^2 , is less than 10%; Trenti & Stiavelli 2008; Casey et al. 2023). These particularly distant and bright galaxies are

prime candidates to constrain the early growth of structures and galaxy formation and evolution models (Finkelstein et al. 2023; Mason et al. 2023; Yung et al. 2024). In addition, this wide area can uniquely probe the different environments in terms of galaxy density and spatial ionization of neutral hydrogen.

The EoR, finishing around $z \sim 6$ (Stanway et al. 2003) with a mid-point at $z = 7.7 \pm 0.8$ (Planck Collaboration et al. 2020), marks a crucial period in the history of the Universe, when the first stars and galaxies formed and started to emit UV radiation that ionized the neutral hydrogen gas in the intergalactic medium (IGM). Quantifying key properties of these galaxies, such as their UV magnitude (M_{UV}), star formation rates (SFRs), stellar masses (M_*), and UV beta (β) slope, can provide valuable insights into these processes. Recent studies have highlighted the importance of the host dark matter halos and the sources that ionized the IGM during the EoR in shaping the properties of the first galaxies (e.g., Hutter et al. 2021).

In this paper, we identify 15 new high- z ($z \geq 9$) galaxy candidates in the first epoch of COSMOS-Web (4% of the total survey area), and employ a range of spectral energy distribution (SED) fitting techniques to accurately derive their physical properties in the early Universe. In Section 2, we outline the observations used for the detection of these galaxies, and we describe the selection method in Section 3. We present the sample and the results of our SED fitting in Section 4, the UV luminosity function in Section 5, and the implications of these results on our understanding of early galaxy growth evolution in Section 6. Throughout this paper, we adopt a spatially flat Lambda cold dark matter (Λ CDM) cosmological model with $H_0 = 70 \text{ km s}^{-1} \text{ Mpc}^{-1}$, $\Omega_m = 0.3$, and $\Omega_\Lambda = 0.7$. We assume a Chabrier (2003) initial mass function (IMF). All magnitudes are quoted in the AB system (Oke & Gunn 1983).

2. Observations and Data Reduction

2.1. The COSMOS-Web Survey

The COSMOS-Web survey (GO #1727; Casey et al. 2023) was selected as a 255 hr JWST treasury program. The full survey will map a contiguous 0.54 deg^2 area using NIRCam and 0.19 deg^2 using the Mid-Infrared Imager (MIRI) in the COSMOS field (Scoville et al. 2007; Capak et al. 2007; Koekemoer et al. 2007). It is the largest JWST (non-pure-parallel) program both in terms of area covered and General

Observer (GO) time allocated. The depths of the NIRCcam data are measured to be 26.9–27.5 AB (F115W), 27.1–27.7 (F150W), 27.7–28.3 (F277W), and 27.6–28.2 (F444W) for 5σ point sources calculated within $0.15''$ radius apertures. For the MIRI/F770W filter, the depths calculated within $0.3''$ radius apertures vary between 25.33 and 25.98 AB for point sources. The variable depth is caused by different portions of the mosaic being covered with a different number of exposures, as the mosaicing of COSMOS-Web uses the somewhat large 4TIGHT dither pattern. More details about the design and motivation for the COSMOS-Web survey are given in Casey et al. (2023).

The first 4% of data (six of 152 visits) for COSMOS-Web were taken in early 2023 January and cover a total area of ~ 77 arcmin² with NIRCcam (~ 8.7 arcmin² of which is also covered by the MIRI parallels). This paper focuses on sources discovered in this initial imaging area.

2.1.1. NIRCcam

As part of COSMOS-Web, observations were taken through the four NIRCcam wide-band filters: F115W, F150W, F277W, and F444W. The full data reduction will be described in detail in M. Franco et al. (2024, in preparation), with the main steps summarized here. After retrieving all the uncalibrated NIRCcam images from the STScI MAST Archive,⁴³ the images were reduced using the JWST Calibration Pipeline version 1.8.3 (Bushouse et al. 2023),⁴⁴ with the addition of several custom modifications, as has also been done for other JWST studies (e.g., Finkelstein et al. 2022; Bagley et al. 2024), including correcting the $1/f$ noise and subtraction of low-level background. We used the Calibration Reference Data System (CRDS) pmap 0989, which corresponds to the NIRCcam instrument mapping imap 0232, where some reference files include in-flight data, and which represented the most current calibrations when our observations were obtained.⁴⁵

The final mosaics are created in stage 3 of the pipeline, which vary only in resolution with a pixel size of $0.03''$ pixel⁻¹ and $0.06''$ pixel⁻¹. Unless otherwise stated, we will use the $0.03''$ pixel⁻¹ resolution mosaic in the following.

Achieving precise absolute and relative astrometry of the JWST mosaics across all the filters is essential for ensuring the reliability of the resulting measurements, including photometry, morphology, and photometric redshift determination. Our astrometric calibration is carried out by utilizing the JWST TweakReg procedure, which is part of the JWST pipeline. To carry out this step, we first generated a reference catalog over our COSMOS-Web region using a new $0.03''$ pixel⁻¹ mosaic of the original COSMOS Hubble Space Telescope (HST) F814W imaging data, which had been reprocessed following the methodology described in Koekemoer et al. (2011), in particular with improved astrometric alignment to Gaia Data Release 3 (Gaia Collaboration et al. 2021) and the COSMOS2020 catalog (Weaver et al. 2022). Our NIRCcam data are aligned to this reference catalog with median offsets in R.A. and decl. below the level of 5 mas, regardless of the filter used, and the median absolute deviation values are less than 12 mas across the entire field, with minor variation between the

different filters (more details will be provided in M. Franco et al. 2024, in preparation).

2.1.2. MIRI

The MIRI parallels taken in conjunction with NIRCcam imaging in 2023 January cover a total area of 27 arcmin², and to date 8.7 arcmin² of that coverage directly overlaps with the NIRCcam imaging. MIRI data were processed through the JWST Calibration Pipeline version 1.8.3, with a two-step procedure (see S. Harish et al. 2024, in preparation). In the first step, we process the MIRI data through stages 1–3 of the JWST pipeline, with in-flight calibrations applied, and obtain the drizzled mosaic image. Then we detect sources in the mosaic image using SExtractor Classic (Bertin & Arnouts 1996) and build a source emission catalog. We mask out pixels of the source emission in the “rate” observations (source-emission-masked rate, or “dark rate”), then for each data set we build a master background rate image by combining dark rate images of other data sets with the same filter and close dates. In the second step, we reprocess the “rate” image of each data set by using the corresponding master background rate image as the background exposure in stage 2 of the JWST pipeline. Then stage 3 of the JWST pipeline produces our final drizzled mosaic, with astrometry aligned to that of the new HST and COSMOS2020 catalogs (same as for NIRCcam).

2.2. Complementary Data

In addition to the JWST data described above, we take advantage of the rich multiwavelength data available across the COSMOS field. In this paper, we make use of HST imaging (Koekemoer et al. 2007), consisting of ACS F814W imaging to an average $\sim 5\sigma$ point source depth of 27.2 AB mag (in a $0.24''$ diameter aperture). We also use the wealth of ground-based optical/near-IR (OIR) imaging data including Subaru Suprime-Cam and Hyper Suprime-Cam imaging (Aihara et al. 2022) as well as UltraVISTA (McCracken et al. 2012) near-IR imaging Data Release 5 (DR5). The details of the ancillary ground-based imaging are described in detail in Weaver et al. (2022), though they make use of UltraVISTA Data Release 4 rather than DR5. In addition to the extensive OIR data in the field, we also use long-wavelength data (submillimeter through radio) as well as X-ray to check for possible emission around the newly identified sources in this work; these data sets are further described in Casey et al. (2023).

3. Methods

3.1. Photometry and SED Fitting

Our methodology involves utilizing SourceExtractor++ (SE++; Bertin et al. 2020; Kümmel et al. 2020), an updated version of the widely used SExtractor package (Bertin & Arnouts 1996), to conduct source detection, model-based photometry, and generate multiband catalogs. We choose to use SE++ model-based photometry in order to take full advantage of the depth and filter coverage of seeing-limited ground-based data in COSMOS and high-resolution near-IR JWST imaging. To detect sources, we construct a χ^2 detection image from all four NIRCcam bands and use priors for the source centroid positions derived from this image. For each detected source in the χ^2 image, SE++ then fits a two-dimensional Sérsic model convolved with the filter-specific

⁴³ <https://archive.stsci.edu/>

⁴⁴ <https://github.com/spacetelescope/jwst>

⁴⁵ <https://jwst-crds.stsci.edu>

Table 1
Photometry of the $z \geq 9$ Galaxy Candidate Sample

ID	R.A.	Decl.	HST/	JWST/	JWST/	JWST/	JWST/	JWST/
(1)	J2000	J2000	F814W	F115W	F150W	F277W	F444W	F770W
(1)	(2)	(3)	(4)	(5)	(6)	(7)	(8)	(9)
COS-28841	149.94791615	2.46773220	>27.55	>27.68	26.64 ± 0.11	26.79 ± 0.07	26.65 ± 0.07	...
COS-17810	149.96667829	2.38852142	>27.54	>28.00	27.10 ± 0.12	26.93 ± 0.06	26.94 ± 0.07	...
COS-29145	149.95579364	2.47287402	>27.55	>27.68	26.88 ± 0.13	27.18 ± 0.10	26.82 ± 0.08	...
COS-5208	149.96468292	2.31632995	>27.54	>27.81	27.06 ± 0.14	27.68 ± 0.14	26.74 ± 0.09	...
COS-12915	149.90581503	2.35780491	>27.67	>28.00	27.02 ± 0.11	27.47 ± 0.10	27.70 ± 0.13	...
COS-21764	149.91077923	2.41372492	>27.77	>28.00	27.16 ± 0.13	27.78 ± 0.13	27.16 ± 0.08	...
COS-26097	149.92357696	2.44227575	>27.53	>27.68	27.24 ± 0.18	27.53 ± 0.13	27.58 ± 0.16	...
COS-22493	149.95203282	2.41836544	>27.56	>27.68	27.36 ± 0.20	27.43 ± 0.12	27.19 ± 0.11	...
COS-12634	149.90414975	2.35610310	>27.76	>27.68	27.42 ± 0.21	27.62 ± 0.14	27.77 ± 0.19	...
COS-14608	149.97992311	2.36788542	>27.41	>27.42	27.30 ± 0.23	27.50 ± 0.17	26.99 ± 0.12	...
COS-4396	149.91345122	2.31169605	>27.59	>28.00	27.40 ± 0.16	27.83 ± 0.13	27.20 ± 0.09	>26.25
COS-24512	150.01008463	2.43176823	>27.48	>27.68	27.17 ± 0.17	28.04 ± 0.21	28.29 ± 0.29	...
COS-10016	149.91281685	2.34193317	>27.58	>27.68	27.41 ± 0.21	27.97 ± 0.19	27.61 ± 0.16	...
COS-21431	149.95684396	2.41151565	>27.56	>27.68	27.65 ± 0.26	28.30 ± 0.25	27.43 ± 0.14	...
COS-3755	149.90714647	2.30812336	>27.54	>28.00	27.89 ± 0.24	28.34 ± 0.21	28.32 ± 0.22	>26.53

Notes. Coordinates and multiband photometry of our galaxy sample with fluxes obtained from SE++ model-based photometry. The limits indicated for F814W, F115W, and F770W correspond to 3σ . No fluxes (above 2σ) have been detected in filters blueward of the supposed Ly α break. VISTA *YJHK_s* are not constraining for these sources; we have omitted them when fitting.

point-spread function (PSF) in each of the measurement bands (see M. Shuntov et al. 2024, in preparation) using a PSF from WebbPSF (Perrin et al. 2014).

We note that, even for sources that are not detected in a given band, SE++ always fits a model, though the model will be below the noise. In this case, computing photometric uncertainties is a nontrivial task, and errors in the dropout bands can sometimes be significantly underestimated. To address this issue, we set a noise floor for each band that corresponds to the rms measured in circular apertures with radii of 0.15'' (for ACS/NIRCam), 0.3'' (for MIRI), and 1'' (for ground-based data). We adopt the measured depths from Weaver et al. (2022) and Casey et al. (2023). The full explanation of the catalog creation will be provided in detail in an upcoming paper (M. Shuntov et al. 2024, in preparation). The IDs of the high-redshift galaxy candidates and the fluxes are given in Table 1. Although each of these fits incorporates slightly different physical assumptions, the diverse range of approaches employed in this study provides a valuable means of testing the validity of the candidate galaxies at $z \geq 9$.

We use several different SED-fitting techniques to derive the redshifts and the properties of our galaxies. We use the EAZY (Brammer et al. 2008), BAGPIPES (Carnall et al. 2018), and BEAGLE (Gutkin et al. 2016; Chevallard & Charlot 2016) SED-fitting tools, with the parameters given in the following sections. We compare the results coming from these different approaches in Section 4.

3.1.1. EAZY

To compute photometric redshifts to initially select our galaxies, we use the SED-fitting tool EAZY. For this purpose, we use the default Flexible Stellar Population Synthesis (FSPS) templates (specifically, the fsp_s QSF 12 v3 version; Conroy & Gunn 2010), and supplement them with six additional templates from Larson et al. (2023) optimized for selecting galaxies at $z > 8$ with JWST. These templates are more effective in replicating the blue UV slopes exhibited by galaxies with high redshifts (see Figure 4 in Larson et al. 2023).

They have been created by integrating stellar population spectra from BPASS (Eldridge & Stanway 2009) with the possibility of incorporating nebular emission data obtained from CLOUDY v17.00 (Ferland et al. 2017) with a high ionization parameter ($\log_{10}(U) = -2$), low gas-phase metallicities ($Z = 0.05 Z_{\odot}$), and excluding Ly α emission. We assume a flat redshift (and magnitude) prior, and we extend the redshift search between 0.01 and 15 with steps of $\Delta z = 0.01$. As is common practice in the literature (e.g., Harikane et al. 2022; Finkelstein et al. 2023) we additionally perform an EAZY run with a maximum redshift of $z = 7$ to compare the best chi-squared between the low- and high-redshift runs.

3.1.2. BAGPIPES

In order to assess the results for photo- z with an alternative procedure, we employ an alternative SED-fitting tool, BAGPIPES (Carnall et al. 2018). Our SED fitting is carried out using a delayed exponentially declining star formation history (SFH) model, where the SFR follows a functional form of $\text{SFR}(t) \propto t \exp(-t/\tau)$. We slightly modify the publicly available BAGPIPES code to parameterize the age of the delayed- τ SFH as a fraction of the Hubble time at redshift z , rather than an absolute age in Gyr. This is necessary to provide equal weight to both old and young stellar populations while maintaining a uniform redshift prior. We assume a Calzetti law (Calzetti et al. 2000) for dust attenuation and BC03 (Bruzual & Charlot 2003) models. Absolute attenuation in the V band can vary between 0 and 3 magnitudes. The ionization parameter can vary between 10^{-3} and 10^{-1} , the stellar mass formed between $10^7 M_{\odot}$ and $10^{11} M_{\odot}$, and the metallicity between 0.001 and 1 times the solar metallicity. We have incorporated nebular emission into our study by utilizing the updated CLOUDY models.

3.1.3. BEAGLE

We also utilized the Bayesian tool BEAGLE, developed by Chevallard & Charlot (2016), to conduct an additional SED fitting. The templates used by BEAGLE were created by Gutkin et al. (2016) and are based on the 2016 updated version of the

BC03 stellar population models and nebular emission calculated using the CLOUDY photoionization code (Ferland et al. 2017). Following others in the literature (e.g., Whittler et al. 2023), we adopted a constant SFH model and log-uniform priors on the total stellar mass ($\log_{10}(M_*/M_\odot)$ from 5 to 10), the maximum stellar age ($\log_{10}(t/\text{yr})$ from 7 to 10), and the stellar metallicity ($\log_{10}(Z/Z_\odot)$ from -2.2 to -0.3). We include dust attenuation following an SMC law with τ_V varying with a log-uniform prior from 0.001 to 5. Finally, we include nebular emission with the ionization parameter $\log_{10}(U)$ varying from -4 to -1 . Crucially, we allow a variable Lyman continuum escape fraction f_{esc} . This allows for young stellar populations with minimal nebular continuum, extending the parameter space covered by the models to bluer UV slopes.

3.1.4. Dense-Basis

We further perform SED fitting for each source using the Dense-Basis SED-fitting code (Iyer & Gawiser 2017) to explore the effects of a nonparametric SFH on the recovered physical parameters. Dense-Basis uses a flexible SFH represented by a Gaussian mixture model (Iyer et al. 2019). For this work, we define three “shape” parameters that describe the SFH: t_{25} , t_{50} , and t_{75} (requiring the recovered SFH of the galaxy to form “ x ” fraction of its total mass by time t_x). We impose a uniform (flat) prior on the specific star formation rate (sSFR) with limits on the sSFR ($\text{sSFR yr}^{-1} \in [10^{-14}, 10^{-7}]$), an exponential prior on the dust attenuation over a wide range of values ($A_V \in [0, 4]$), and a uniform (in log-space) prior on the metallicity ($Z/Z_\odot \in [0.01, 2.0]$). All sources were fit with Dense-Basis assuming a Calzetti dust attenuation law and a Chabrier IMF. We further constrain the redshift range to within 1σ of the BEAGLE best-fit redshift to generate posteriors on the galaxies’ physical properties under the assumption that redshifts are accurately recovered by BEAGLE. We use this method to derive the stellar mass and the SFR.

3.2. Selection of $z \geq 9$ Galaxy Candidates

In this paper, we focus on the detection of galaxies with $z \geq 9$. At these redshifts, the Ly α break is certain to lie in one of the JWST filters, starting from F115W for a $z = 9$ galaxy and shifting to redder filters for higher-redshift galaxies. This allows us to identify the drop in flux due to the Ly α break using only NIRCcam filters, rather than requiring another instrument such as HST (as would be the case for lower-redshift galaxies with a Ly α break at shorter wavelengths). Due to the high sensitivity of NIRCcam, this allows us to both reliably identify the presence of a break (thus constructing a robust sample) and measure the Δ (magnitude) across the break that is used to derive galaxy physical properties. This selection method is particularly advantageous for the reliable selection of $z \geq 9$ galaxies.

We construct our sample of high-redshift candidates inspired by the method described in Finkelstein et al. (2023). We employ the following criteria. We require:

1. A best-fit photometric redshift (z_a) > 8.9 from EAZY.
2. A robust detection in the two long-wavelength filters. We impose a S/N > 5 measured in $0.2''$ diameter apertures in F277W and F444W.
3. A S/N < 2 in bands blueward of the supposed Ly α break.

4. $\int \mathcal{P}(z < 9) dz \leq 0.3$ with EAZY. This means that more than 70% of the integrated probability is above $z \geq 9$.
5. A goodness-of-fit $\chi^2/N_{\text{filt}} < 3$ with EAZY, where $N_{\text{filt}} = 5$, the number of filters that effectively constrain the redshift measurement, here F814W, F115W, F150W, F277W, and F444W.
6. A significantly better fit for the entire redshift range than for redshifts restricted between 0 and 7, defined as $\Delta\chi^2 > 2$.
7. A radius (determined by SE++) greater than $0.01''$ to remove bad or hot pixels.

This selection is intentionally restrictive but does not require extensive visual inspection after these filters have been applied (though all sources that fulfill these criteria were visually inspected). This serves as a pilot study of $z \geq 9$ sources in COSMOS-Web and will be superseded with a larger-scale study when all survey data are in hand. Our selection criteria result in a total of 15 $z \geq 9$ candidates. We have differentiated in the rest of this study the galaxies for which the redshift is the most reliable with a $\Delta\chi^2$ between the high-redshift and low-redshift solutions of EAZY greater than 8 (five galaxies) compared with galaxies with $\Delta\chi^2 \leq 8$ (10 galaxies). We advocate for the use of this value to enable direct comparisons between surveys (e.g., CEERS; Finkelstein et al. 2023). Note that the quantity χ^2 is not reduced. We double-checked that the sources were not previously detected with the Atacama Large Millimeter/submillimeter Array using the A³COSMOS catalog (data version 20200310; Liu et al. 2019) nor with the Very Large Array at 3 GHz (Smolčić et al. 2017) within a radius of $0.9''$.

4. Results

In Table 2, we summarize the redshifts of our 15 candidates from each of the SED-fitting approaches. We also show the goodness-of-fit based on the χ^2 between the EAZY fits when run in full and low- z modes, respectively.

4.1. The Sample

Here, we present our sample of $z \geq 9$ galaxies selected in the first COSMOS-Web data set. Figure 1 shows a color image of the COSMOS field in the four NIRCcam bands, with the positions of our 15 $z \geq 9$ candidates overlaid.

In Figure 2, we show the best-fitting UV-optical SEDs of the galaxies, along with their redshift probability distribution functions (PDFs). We show cutout stamps for each galaxy above the SED, from HST/F814W to MIRI/F770W in the Appendix (see Figure A1). In all cases, the galaxy emission becomes more prominent toward redder wavelengths, with clear detections in the NIRCcam F150W–F444W bands.

4.2. Properties of $z \geq 9$ Galaxy Candidates

In this section, we discuss the properties of this sample of $z \geq 9$ galaxies. In Table 3, we summarize the stellar masses, UV magnitudes, β slopes, SFRs, dust attenuations A_V , radii, and Sérsic indices for our sample.

4.2.1. Redshift

The best-fit photometric redshifts derived by EAZY, BEAGLE, and BAGPIPES are shown in the top-right corner of each panel in Figure 1, in addition to the redshift PDF in the upper-left

Table 2
Measurements of Redshifts

ID (1)	z_{EAZY} (2)	χ^2_{EAZY} (3)	$\chi^2_{\text{EAZY,low-z}}$ (4)	$\Delta\chi^2_{\text{EAZY}}$ (5)	z_{BEAGLE} (6)	z_{BAGPIPES} (7)
COS-28841	$10.2^{+0.3}_{-0.6}$	4.6	21.1	16.5	$10.9^{+0.2}_{-0.2}$	$9.9^{+0.3}_{-0.4}$
COS-17810	$10.9^{+0.3}_{-0.5}$	9.1	13.4	4.3	$10.9^{+0.3}_{-0.3}$	$10.7^{+0.2}_{-0.4}$
COS-29145	$9.5^{+0.7}_{-0.5}$	5.4	14.7	9.4	$9.7^{+0.4}_{-0.4}$	$9.6^{+0.4}_{-0.4}$
COS-5208	$8.9^{+0.8}_{-0.2}$	9.9	24.9	14.9	$10.6^{+0.3}_{-0.2}$	$8.8^{+0.2}_{-0.3}$
COS-12915	$10.0^{+0.4}_{-0.7}$	4.1	24.3	20.3	$9.8^{+0.4}_{-0.4}$	$9.7^{+0.3}_{-0.3}$
COS-21764	$9.4^{+0.4}_{-0.6}$	13.5	21.2	7.7	$10.6^{+0.3}_{-0.2}$	$9.1^{+0.5}_{-0.3}$
COS-26097	$10.2^{+0.5}_{-1.0}$	3.9	8.2	4.4	$10.0^{+0.4}_{-0.4}$	$9.8^{+0.4}_{-0.5}$
COS-22493	$9.0^{+1.0}_{-6.3}$	4.2	6.9	2.7	$9.5^{+0.6}_{-0.4}$	$9.2^{+0.7}_{-0.6}$
COS-12634	$10.3^{+0.5}_{-1.2}$	1.6	6.4	4.9	$9.9^{+0.6}_{-0.6}$	$9.8^{+0.6}_{-0.5}$
COS-14608	$9.7^{+0.6}_{-3.6}$	4.3	6.6	2.3	$9.7^{+0.5}_{-0.5}$	$9.4^{+0.6}_{-1.1}$
COS-4396	$9.9^{+0.7}_{-0.7}$	1.0	16.1	15.1	$10.0^{+0.3}_{-0.4}$	$9.7^{+0.4}_{-0.4}$
COS-24512	$9.8^{+0.5}_{-0.6}$	6.1	12.4	6.3	$9.7^{+0.3}_{-0.4}$	$9.1^{+0.8}_{-7.0}$
COS-10016	$9.0^{+1.1}_{-1.4}$	3.2	6.6	3.4	$9.5^{+0.6}_{-0.6}$	$9.1^{+0.8}_{-2.0}$
COS-21431	$9.5^{+0.6}_{-1.5}$	4.8	8.2	3.3	$9.3^{+0.5}_{-0.5}$	$8.8^{+0.9}_{-1.2}$
COS-3755	$9.6^{+1.2}_{-0.8}$	0.9	5.2	4.3	$9.6^{+0.6}_{-0.5}$	$9.7^{+0.6}_{-2.5}$

Note. Column (1): ID; column (2): photometric redshifts from EAZY; columns (3) and (4): the χ^2 values from EAZY with a redshift between 0 and 15 and EAZY with a redshift range set to be $z < 7$, called the “low- z ” solution, respectively; column (5): the difference in χ^2 between these two EAZY runs; columns (6) and (7): the best redshift solutions from BEAGLE and BAGPIPES, respectively.

corner of each panel. The redshift of our sample (from EAZY) varies between 9.2 and 10.7. This means that we selected only F115W dropouts. No galaxy in our sample is a F150W dropout. We find good agreement between the different redshift estimations (see Figure 3). All derived redshifts, regardless of the technique, are in agreement within their uncertainties. For this sample, we find a difference $\Delta z / (1 + z_{\text{mean}})$ of 0.02 between BAGPIPES and EAZY, 0.05 between BEAGLE and BAGPIPES, and 0.02 between BEAGLE and EAZY. BAGPIPES gives systematically slightly lower redshifts than the two other SED-fitting codes.

Without spectroscopic confirmation of these sources, there may be doubts about the reliability of these redshifts. Since the publication of the first studies on Lyman break galaxy (LBG) candidates at $z > 10$, concerns have been raised that some of these candidates may be low-redshift dusty contaminants (e.g., Zavala et al. 2023), which could significantly impact our understanding of early galaxy formation. While spectroscopic redshifts are now trickling in at $z \sim 9$ –13 (e.g., Arrabal Haro et al. 2023a, 2023b; Fujimoto et al. 2023; Curtis-Lake et al. 2023; Robertson et al. 2023; Roberts-Borsani et al. 2023; Boyett et al. 2024), most high-redshift candidates still exhibit secondary redshift solutions at $z \sim 3$ –6. Recently, Arrabal Haro et al. (2023a) have shown that the galaxy previously claimed to have the highest photometric redshift (CEERS-93316, $z_{\text{phot}} \sim 16$; Donnan et al. 2023b) was, in fact, at $z_{\text{spec}} = 4.9$, with an SED exhibiting the signature of a dusty star-forming galaxy (DSFG), with strong nebular lines mimicking the Ly α break. Models often make the assumption that these galaxies have a red color that sets them apart from the typically blue LBGs. The intricate interstellar medium (ISM) environments present in DSFGs (see review by Casey et al. 2014) along with contamination from nebular emission lines could result in a variety of observed near-IR colors (Naidu et al. 2022; Pérez-González et al. 2023; Zavala et al. 2023; McKinney et al. 2023). However, we used a selection technique relatively similar to (but with a different number of filters and depth) that used in the CEERS field (Finkelstein et al. 2023); Fujimoto et al. (2023) achieve a

spectroscopic confirmation rate of $\sim 90\%$ for galaxies with $z \sim 8$ –9. It is interesting to note that in this latter study, the photometric redshifts (derived with EAZY) are for the most part (six out of seven) higher (by $\Delta z \sim 1$ –2) compared to the spectroscopic redshifts that were determined afterwards.

Comparison with the CEERS survey is nontrivial because its greater number of filters and increased depth compared to COSMOS-Web. To address this, we performed a detailed quantitative analysis to evaluate the uncertainties arising from these differences in filter count and survey depth. We adopted the CEERS multiband SExtractor catalog (version 0.51) described in Finkelstein et al. (2022) and executed the EAZY photometric redshift code for all CEERS filters, applying the same parameters as in our primary analysis. To simulate the depth difference, we then selected only the four NIRCcam filters and the MIRI filter used by COSMOS-Web and incorporated the COSMOS-Web flux errors in quadrature for these filters. We then reexecuted EAZY again. Our comparison focused on galaxies meeting our study’s criteria ($\text{mag}_{\text{F277W}} < 28.3$ AB and $9 < z < 12$). The resultant redshift differences between the two approaches were analyzed, yielding a median redshift difference of $(z_{\text{CEERS}} - z_{\text{COSMOS-Web}}) / z_{\text{CEERS}} = 0.0054$. This validates the general reliability of the photometric redshift estimates out to $z \sim 9$, close to the redshift range of our sample.

4.2.2. UV Magnitudes and Spectral Slopes

The rest-frame UV spectrum of a galaxy can be approximated with a power law of the form $f_{\lambda} \propto \lambda^{\beta}$ (Calzetti et al. 1994; Meurer et al. 1999). Pre-JWST studies performed at high redshift ($z > 6$) with HST have shown that the galaxies presented blue UV slopes with slope values near -2 (e.g., Finkelstein et al. 2012; Bouwens et al. 2014), typical of relatively young and metal-poor galaxies. The main question is to know if at higher redshift we observe an abrupt break of slope that can reach values of -3 , as has been reported recently by Topping et al. (2022), Cullen et al. (2023), and Austin et al. (2023). We calculated the β slope of these galaxies by fitting a

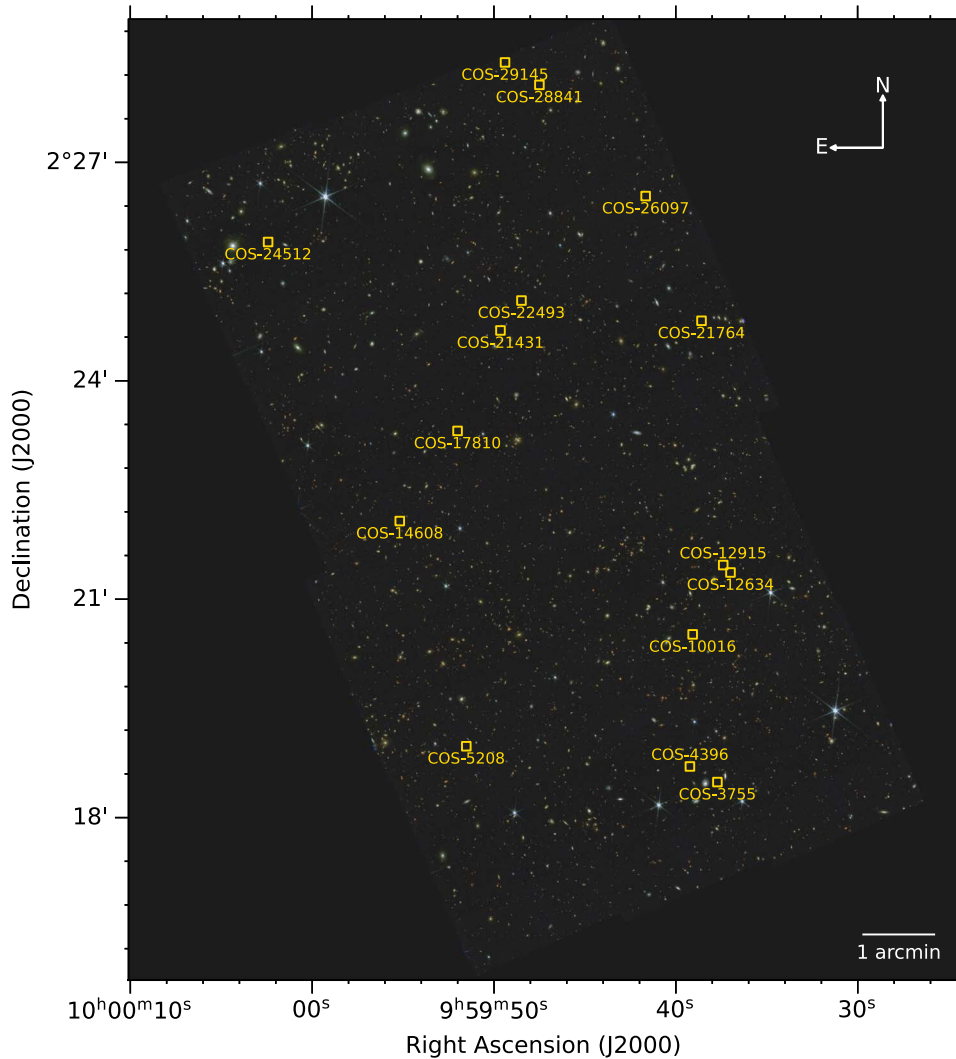


Figure 1. JWST/NIRCam color image (F115W, F150W, F277W, and F444W) of the first six visits (out of a total of 152) of COSMOS-Web. The positions of our 15 high- z galaxy candidates are indicated by the yellow squares.

power law to the best-fit spectrum from BEAGLE between 1268 and 2580 Å using the fitting windows given in Table 2 of Calzetti et al. (1994). This method has proven its efficiency and accuracy and gives better results than the use of a single color, for example, which is much more subject to photometric outliers. In addition, it is the method with the smallest dispersion when compared with simulations (Finkelstein et al. 2012). The uncertainties were calculated by generating 800 fits from the posterior and considering the 16th to 84th percentiles. The rest-frame UV slope for our sample ranges between -2.0 and -2.7 (mean value -2.4), with UV magnitudes from -19.5 to -21.2 . To compare the different studies, it is necessary to put them in perspective with the UV magnitude.

Indeed, many studies point out the evolution of the β slope as a function of UV magnitude (e.g., Bouwens et al. 2014; Cullen et al. 2023). This would suggest that the brighter galaxies are also older, more dust-obscured, and more metal-enriched than the fainter ones (i.e., Cullen et al. 2023). Due to the large contiguous area of the COSMOS-Web survey, it will be possible to explore a wider portion of the parameter space by finding rarer galaxies with brighter UV magnitudes than other studies. We calculate the absolute magnitude at 1500 Å

using the best-fit spectrum from BEAGLE. This involves integrating the flux within a 100 Å-wide top-hat filter centered on 1500 Å and then conversion to apparent magnitude (m_{1500}). We then convert it to an absolute magnitude following

$$M_{UV} = m_{1500} - 5 \log_{10} \left(\frac{D_L}{10} \right) + 2.5 \log_{10}(1 + z), \quad (1)$$

with D_L the luminosity distance in parsecs. We have verified that the results given by the different SED-fitting tools are consistent with each other. The β and M_{UV} values are consistent within ~ 0.2 .

In Figure 4, we show the evolution of the absolute UV magnitude as a function of redshift for our sample and for a compilation of galaxies detected with JWST at $z > 8.5$ (Naidu et al. 2022; Finkelstein et al. 2023; Donnan et al. 2023b; Harikane et al. 2023; Bradley et al. 2023; Austin et al. 2023; Castellano et al. 2022, 2023; Atek et al. 2023a, 2023b; Bouwens et al. 2023; Arrabal Haro et al. 2023a, 2023b; Curtis-Lake et al. 2023; Bunker et al. 2023; Roberts-Borsani et al. 2023; Williams et al. 2023; Cameron et al. 2023; Fujimoto et al. 2023; Larson et al. 2023; Tang et al. 2023). For

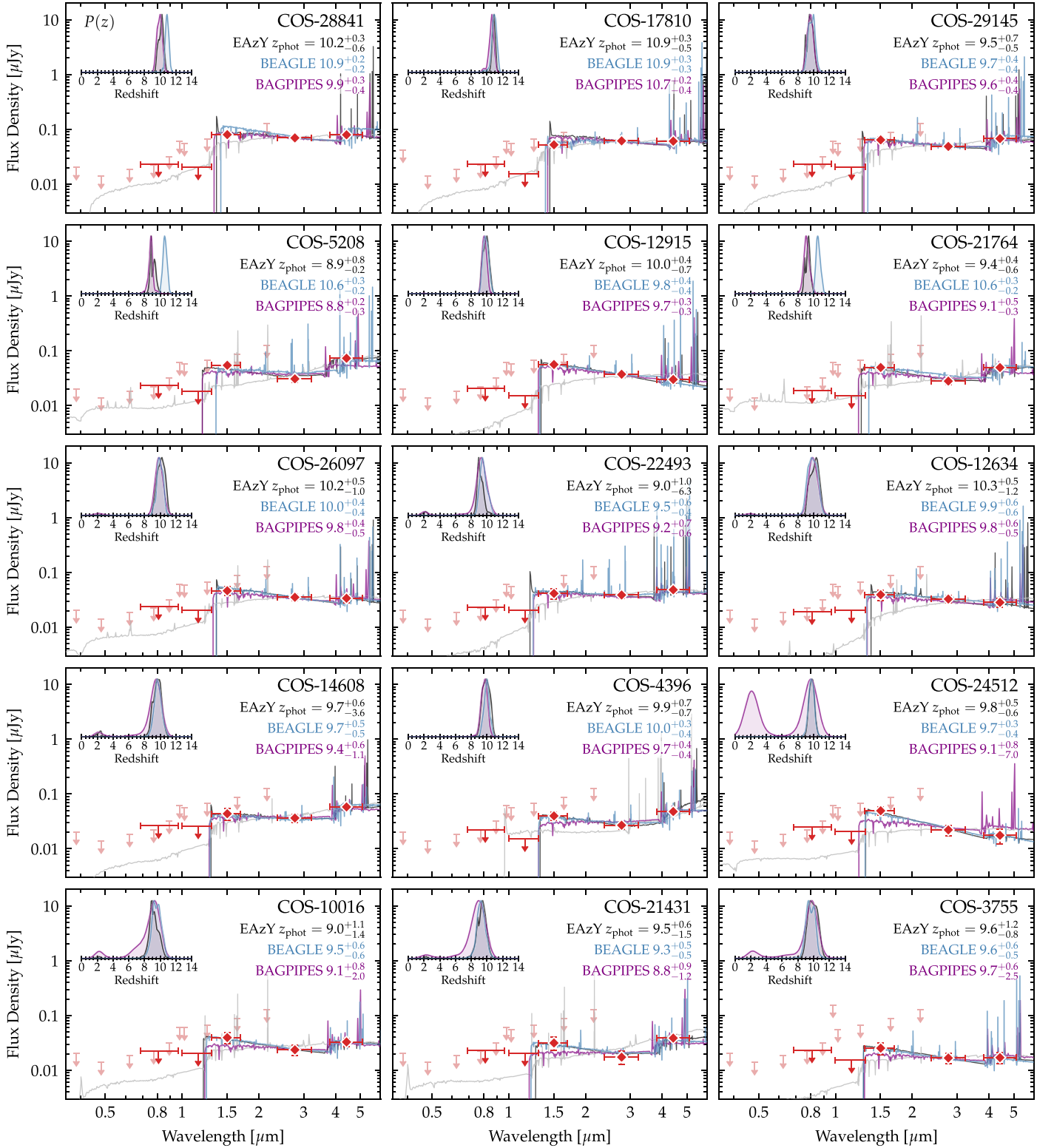


Figure 2. Main panels: spectral energy distributions ordered by M_{UV} (bright to faint). Redshift probability distributions are shown in the top left on each panel, and the redshifts themselves are given in the top right for each SED-fitting code (dark gray, EAZY; blue, BEAGLE; purple, BAGPIPES). Best-fitting SED model templates for each code are also shown with the same color-coding (we add in addition in light gray the low- z solution, $z < 7$, from EAZY). Red points, and 2σ limits, are observed data.

the redshift range of our study ($z \sim 9-11$), our sample is among the galaxies with the brightest UV magnitude. In particular, the two most distant galaxies in this sample are exceptionally bright (COS-28841 and COS-17810), with $M_{UV} = -21.21^{+0.11}_{-0.11}$

and $-20.94^{+0.19}_{-0.13}$, respectively. These two galaxies are slightly fainter than GN-z11 ($M_{UV} = -21.50 \pm 0.02$; Bunker et al. 2023), one of the most luminous galaxies detected at these redshifts.

Table 3
Physical Properties of the $z > 9$ Galaxy Sample

ID	M_{UV} (mag)	β	$\log_{10}(M_*/M_\odot)$ (M_\odot)	SFR ₁₀ ($M_\odot \text{ yr}^{-1}$)	A_V (mag)	R_{eff} (mas)	R_{eff} (pc)	n	age ₅₀ (Gyr)
(1)	(2)	(3)	(4)	(5)	(6)	(7)	(8)	(9)	(10)
COS-28841	$-21.21^{+0.11}_{-0.11}$	$-2.54^{+0.17}_{-0.13}$	$8.8^{+0.3}_{-0.3}$	$13.1^{+2.5}_{-2.8}$	$0.01^{+0.04}_{-0.01}$	111 ± 8	437 ± 33	0.5 ± 0.1	$0.05^{+0.17}_{-0.04}$
COS-17810	$-20.94^{+0.19}_{-0.13}$	$-2.42^{+0.27}_{-0.17}$	$8.9^{+0.5}_{-0.4}$	$8.7^{+7.0}_{-7.0}$	$0.05^{+0.08}_{-0.04}$	137 ± 7	536 ± 29	1.0 ± 0.1	$0.15^{+0.09}_{-0.14}$
COS-29145	$-20.52^{+0.14}_{-0.16}$	$-2.33^{+0.25}_{-0.19}$	$9.5^{+0.2}_{-0.5}$	$8.0^{+3.0}_{-3.8}$	$0.04^{+0.07}_{-0.03}$	61 ± 12	262 ± 52	1.9 ± 0.6	$0.26^{+0.09}_{-0.11}$
COS-5208	$-20.40^{+0.13}_{-0.11}$	$-2.19^{+0.18}_{-0.13}$	$8.8^{+0.5}_{-0.5}$	$6.2^{+1.9}_{-1.6}$	$0.03^{+0.05}_{-0.02}$	130 ± 23	522 ± 94	4.5 ± 1.2	$0.16^{+0.10}_{-0.14}$
COS-12915	$-20.40^{+0.12}_{-0.13}$	$-2.67^{+0.16}_{-0.12}$	$8.4^{+0.3}_{-0.3}$	$5.1^{+1.2}_{-1.1}$	$0.02^{+0.04}_{-0.02}$	96 ± 12	406 ± 51	0.7 ± 0.2	$0.04^{+0.21}_{-0.03}$
COS-21764	$-20.29^{+0.13}_{-0.14}$	$-2.32^{+0.15}_{-0.22}$	$8.5^{+0.5}_{-0.3}$	$5.8^{+1.1}_{-1.1}$	$0.02^{+0.04}_{-0.01}$	148 ± 22	596 ± 91	5.4 ± 1.6	$0.09^{+0.15}_{-0.07}$
COS-26097	$-20.26^{+0.18}_{-0.18}$	$-2.56^{+0.27}_{-0.14}$	$8.6^{+0.5}_{-0.5}$	$6.4^{+1.9}_{-1.2}$	$0.03^{+0.07}_{-0.02}$	82 ± 17	343 ± 71	1.0 ± 0.3	$0.18^{+0.11}_{-0.16}$
COS-22493	$-20.09^{+0.20}_{-0.19}$	$-2.18^{+0.40}_{-0.25}$	$9.0^{+0.4}_{-0.6}$	$8.1^{+3.2}_{-3.1}$	$0.09^{+0.12}_{-0.07}$	73 ± 15	315 ± 66	1.2 ± 0.4	$0.22^{+0.10}_{-0.19}$
COS-12634	$-20.08^{+0.22}_{-0.24}$	$-2.54^{+0.37}_{-0.19}$	$8.5^{+0.5}_{-0.4}$	$4.4^{+1.3}_{-1.6}$	$0.04^{+0.09}_{-0.03}$	71 ± 18	298 ± 77	0.7 ± 0.3	$0.16^{+0.13}_{-0.14}$
COS-14608	$-20.04^{+0.34}_{-0.26}$	$-1.97^{+0.50}_{-0.34}$	$9.3^{+0.3}_{-0.7}$	$3.9^{+5.3}_{-2.8}$	$0.13^{+0.15}_{-0.09}$	78 ± 21	334 ± 91	1.6 ± 0.5	$0.28^{+0.09}_{-0.11}$
COS-4396	$-19.99^{+0.18}_{-0.14}$	$-2.20^{+0.27}_{-0.17}$	$8.4^{+0.4}_{-0.2}$	$7.2^{+1.6}_{-2.3}$	$0.05^{+0.09}_{-0.03}$	50 ± 17	212 ± 71	0.7 ± 0.3	$0.11^{+0.13}_{-0.09}$
COS-24512	$-19.94^{+0.21}_{-0.15}$	$-2.72^{+0.17}_{-0.11}$	$8.3^{+0.4}_{-0.3}$	$3.1^{+0.6}_{-0.5}$	$0.01^{+0.04}_{-0.01}$	48 ± 27	207 ± 115	0.5 ± 0.3	$0.05^{+0.20}_{-0.04}$
COS-10016	$-19.85^{+0.23}_{-0.18}$	$-2.42^{+0.36}_{-0.23}$	$8.5^{+0.5}_{-0.5}$	$4.1^{+0.8}_{-1.0}$	$0.04^{+0.09}_{-0.03}$	55 ± 25	239 ± 109	1.4 ± 0.6	$0.18^{+0.12}_{-0.16}$
COS-21431	$-19.47^{+0.36}_{-0.24}$	$-2.08^{+0.49}_{-0.32}$	$8.6^{+0.5}_{-0.6}$	$1.5^{+1.0}_{-0.9}$	$0.11^{+0.14}_{-0.08}$	61 ± 34	269 ± 151	0.5 ± 0.2	$0.21^{+0.11}_{-0.19}$
COS-3755	$-19.46^{+0.26}_{-0.22}$	$-2.59^{+0.29}_{-0.13}$	$7.3^{+1.5}_{-1.6}$	$2.2^{+0.3}_{-0.7}$	$0.02^{+0.06}_{-0.02}$	67 ± 27	287 ± 117	0.5 ± 0.3	$0.27^{+0.10}_{-0.16}$

Note. Column (1): ID ordered by M_{UV} ; column (2): UV magnitude; column (3): rest-frame UV slopes; column (4): stellar mass; column (5): star formation rate averaged over 10 Myr; column (6): dust attenuation A_V ; columns (7) and (8): radius in milliarcseconds and in parsecs at the redshift (BEAGLE) of the source; column (9): Sérsic index; column (10): the age of galaxy after formation of 50% of its stellar mass.

In Figure 5 (left), we show the evolution of the β slope as a function of redshift. The redshift range of our sample is relatively narrow: $\Delta z \sim 1.5$, corresponding to ~ 100 Myr. Observing a trend can be challenging. We did not find any correlation between M_{UV} and β in our sample. Our results are slightly bluer than the relationship depicted in Figure 5 (right), which is derived from the work of Cullen et al. (2023) by $\Delta\beta \approx -0.4$ but well aligned with the predictions from the THESAN project (Kannan et al. 2021; Garaldi et al. 2022; Smith et al. 2022) simulating the emission-line properties of high-redshift galaxies. Further investigation and a larger sample are needed to understand the origin of these somewhat bluer colors.

We note that the breadths of β slopes measured in this sample are somewhat narrower than literature samples, though this is most likely due to the difference in approach to measuring β : We use the best-fit SED to constrain the slope rather than a direct measurement from photometry. The latter is free from potential bias introduced by the SED fit, but introduces other systematics due to the different rest-frame wavelengths of the bands used to calculate β .

At certain redshifts, dust-obscured galaxies with strong nebular emission lines and high optical attenuation ($A_V > 3-5$) can mimic the photometry of $z \geq 9$ LBGs. In this case, the increase in broadband filter flux by strong optical emission lines can mask the underlying red continuum and give the appearance of a blue UV continuum slope. However, as shown in McKinney et al. (2023), strong lines are only capable of reproducing β up to -1.5 for high- z candidates with $8 < z < 14$ (blue contours, left panel of Figure 5). Our sample falls outside of this confusion regime, which diminishes the likelihood of low-redshift DSFGs contaminating our sample in addition to the success rate of, for example, Fujimoto et al. (2023) as previously discussed.

The bluest galaxy in our sample (COS-24512) has an index $\beta = -2.72^{+0.17}_{-0.11}$. Though quite blue, this steepness is not extreme and is even comparable to values derived in the local

Universe (e.g., NGC 4861, NGC 1705, and Mrk153, with β from -2.5 to -2.4 ; Takeuchi et al. 2012). This would seem to show that even at $z \sim 10$ the stellar population did form from an environment that is not particularly dusty but one that is certainly already enriched in metals. With a mean value of $\beta = -2.4 \pm 0.2$, β seems to be relatively constant between $z = 7$ and $z = 11$ (Dunlop et al. 2013; Bouwens et al. 2014). In contrast to Topping et al. (2022) at $z = 7-8$, or Cullen et al. (2023) and Austin et al. (2023) at higher redshifts, we do not find any ultra-blue objects in our sample. This may mean that the mixing of the ISM may be heterogeneous or the properties of the galaxies may be environment dependent or due to a blue bias in the β scatter at faint luminosities (as suggested by Cullen et al. 2023), and only an observation over a much larger field will reveal this. Even if we do not find extremely blue galaxies, we can still note that our sample is systematically slightly bluer at a given UV magnitude than the relations derived by Cullen et al. (2023) and Bouwens et al. (2014) but are in good agreement with the prediction from the THESAN simulations for $z \sim 9$ galaxies (Kannan et al. 2022; see the right panel of Figure 5).

While we find no significant dependence between the evolution of the UV spectral slope and the redshift or absolute UV magnitude (Pearson $r = -0.13$ and 0.18 , respectively), we observe a correlation between β and stellar mass (Pearson $r > 0.5$); see Figure 6. We relate these two quantities for our sample by the following equation:

$$\beta = (0.24 \pm 0.10) \times \log_{10}(M_*/M_\odot) - 4.42 \pm 0.90. \quad (2)$$

This means that the more massive a galaxy, the redder its UV spectral slope. We want to emphasize that the level of completeness can strongly influence this scenario, as our data set tends to detect low-mass blue galaxies more readily than low-mass red galaxies. The effects of completeness on the type of galaxies detected will be studied in detail in a future paper in preparation. However, this correlation between β and stellar

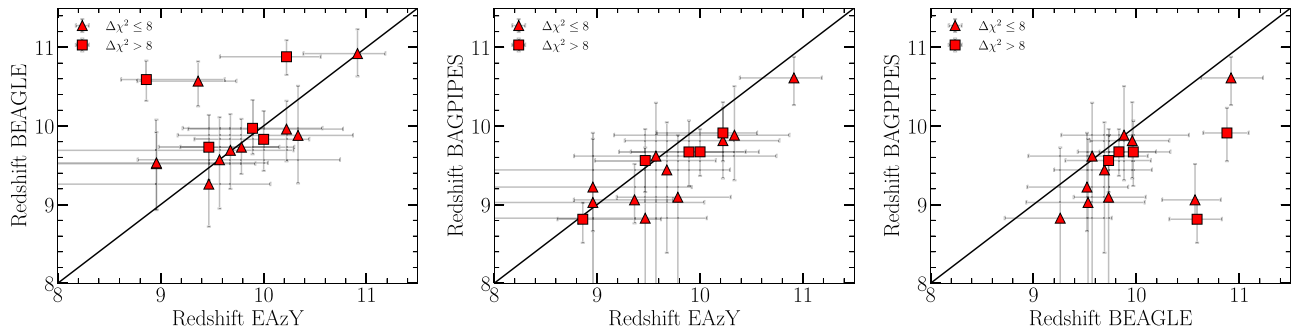


Figure 3. Comparison of the redshift obtained with EAZY, BAGPIPES, and BEAGLE. Differences in the model assumptions, priors, and fitting procedures lead to a difference $\Delta z/(1+z_{\text{mean}})$ 0.02 between BAGPIPES and EAZY, 0.05 between BEAGLE and BAGPIPES, and 0.02 between BEAGLE and EAZY. We can, however, note that BAGPIPES gives a globally lower redshift than the two other codes. We have differentiated our sample in two subsamples according to the EAZY $\Delta\chi^2$ between the high-redshift solution (unconstrained) and the low-redshift solution ($z < 7$) with triangle and square markers. No significant differences have been found between these two subsamples.

mass has also been noted in previous studies (e.g., Finkelstein et al. 2012; Tacchella et al. 2022).

4.2.3. Stellar Masses and Star Formation Rates

All of the galaxies of our sample lie at relatively low stellar mass, as expected for this high redshift, between $\log_{10}(M_*/M_\odot) \sim 8.3\text{--}9.5$, with one outlier at $\log_{10}(M_*/M_\odot) = 7.3$. We also infer low levels of dust obscuration, $A_V < 0.2$ in all cases, with the majority of galaxies with nearly no attenuation, $A_V < 0.1$. However, we emphasize that this value is not well constrained directly due to a degeneracy between the redshift and A_V .

Figure 7 (left) shows the distribution of detected stellar masses as a function of redshift. We have added to these values the predicted contours from extreme value statistics (EVS; Gumbel 1958; Kotz & Nadarajah 2000) derived by Lovell et al. (2023), adapted to the surface area of this survey. This approach predicts the probability contours of the maximum (or minimum) value of a random variable selected from a given distribution. This method has been applied to the halo mass function, in order to derive the most massive halo at a specific redshift (Harrison & Coles 2011), then coupled with a model for the stellar fraction to derive the PDF of the galaxy with the highest stellar mass for a given volume (Lovell et al. 2023). If galaxies were observed to be considerably higher than the anticipated values for the most massive object, it would suggest a conflict with the Λ CDM paradigm, or with the astrophysics underlying the stellar-to-halo mass relation at high redshift. In Figure 7 (left), the dotted line shows the median of the maximum expected stellar mass for a survey of 77.19 arcmin^2 , while the shades of blue show confidence intervals at 1, 2, and 3σ around this value. We assume a baryon fraction of 0.3, and a log-normal distribution of the stellar fraction. The dashed line shows the upper 3σ limit assuming a stellar fraction of unity. At a given redshift interval the most massive galaxy in our sample is globally on that median value, with no galaxy more than 1σ above that limit. This indicates no tension between our observations and the Λ CDM cosmology, nor the astrophysics of galaxy evolution at high redshift.

The average SFRs over 10 Myr derived for this sample of galaxies by the Dense-Basis SED-fitting code are between 1 and $13 M_\odot \text{ yr}^{-1}$. Differences in SFHs from SED-fitting codes may cause these values to vary slightly. Although our values show a wide dispersion, they are in good agreement with the expected values from the hydrodynamic simulation FLARES

(Lovell et al. 2021; Vijayan et al. 2021) at $z \sim 10$ and Santa Cruz semi-empirical simulation (SAM; e.g., Yung et al. 2019) for galaxies at $z = 9.5\text{--}10$ (Figure 8).

4.2.4. Sizes and Morphologies

To characterize the rest-frame optical sizes and Sérsic index of our sample, we utilize SE++. If the measured size uncertainty is less than that derived in Equation (21) of Condon (1997), we rescale the uncertainty according to this equation. Our sample sizes are compact, as none of the galaxies in our sample have an effective radius larger than 0.7 kpc. We find a mean effective radius of $0.37 \pm 0.13 \text{ kpc}$ in F277W, consistent with the rest-frame UV sizes detected in other surveys such as GLASS (Yang et al. 2022) or CEERS (Finkelstein et al. 2023), which have median sizes of 0.41 kpc (F277W) and 0.46 kpc (F200W), respectively. In Figure 9, we show the distribution of sizes as a function of F277W magnitude. Except for the two galaxies with a high Sérsic index ($n \sim 4$), we observe a trend linking magnitude and size, the brightest galaxies being clearly resolved. This correlation could come from the capacity to measure sizes when the S/N is higher, but could also be a physical effect. Recent studies by Marshall et al. (2022) have shown a correlation between galaxy size and far-UV luminosity when measured from dust-attenuated images (this correlation is reversed when the effects of dust are not taken into account) and suggest that dust is the main cause of this correlation. While the two with high Sérsic indices are measured to be spatially resolved on scales of 600–700 pc, larger than the median size of the sample, the uncertainty on their sizes is also higher. We emphasize that there is a selection bias: At a given depth, it is not possible to detect the most extended sources due to the decrease in surface brightness. Figure 9 illustrates the size and magnitude domain that we cannot reach with our survey for different numbers of exposures, specifically two and four (see Section 2), corresponding to over 93% of the survey area. This trend between size and magnitude is also observed in other surveys (e.g., Yang et al. 2022; Finkelstein et al. 2023). In the F277W filter, the PSF is $0.092''$, representing an effective radius of 192 pc at the average redshift of our sample ($z_{\text{mean, BEAGLE}} = 9.98$).

5. UV Luminosity Function

The rest-frame ultraviolet luminosity function (UVLF) is a crucial observational tracer of early galaxy evolution. The measured volume density of UV-luminous galaxies can be

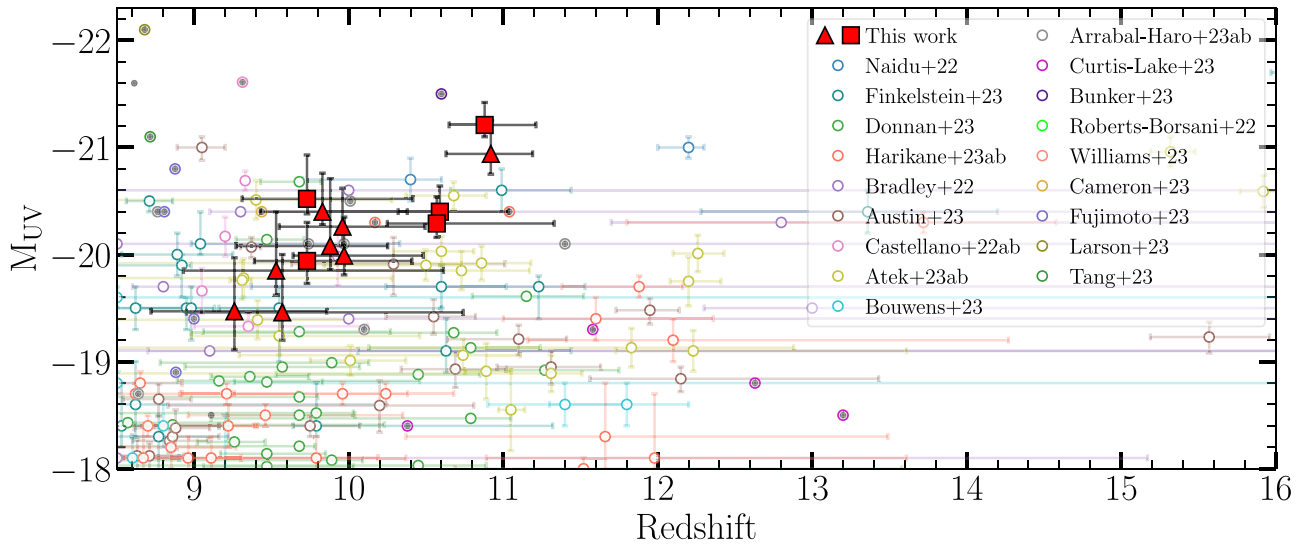


Figure 4. Absolute UV magnitude (M_{UV}) as a function of redshift (BEAGLE) for our $z > 9$ galaxy sample (red points). The difference between red squares and red triangles is the same as in Figure 3. We include data from the literature from Naidu et al. (2022), Finkelstein et al. (2023), Donnan et al. (2023b), Harikane et al. (2023, 2024), Bradley et al. (2023), Austin et al. (2023), Castellano et al. (2022, 2023), Atek et al. (2023a, 2023b), Bouwens et al. (2023), Arrabal Haro et al. (2023a, 2023b), Curtis-Lake et al. (2023), Bunker et al. (2023), Roberts-Borsani et al. (2023), Williams et al. (2023), Cameron et al. (2023), Fujimoto et al. (2023), Larson et al. (2023), and Tang et al. (2023). If a galaxy is mentioned in multiple papers and a spectroscopic redshift is available, we have only displayed the one with spectroscopic confirmation. Otherwise, we have taken a conservative approach and displayed the galaxy with the lowest redshift available. Galaxies with spectroscopic confirmation (line or break) are displayed with an additional black dot. At a given redshift, the galaxies in our sample are generally those that display some of the brightest UV magnitudes.

directly compared to simulations to better understand the physical mechanisms that drive galaxy evolution. Observations from the first year of JWST observations have now grown large enough to allow the direct calculation of the UVLF beyond pre-JWST limits at $z \sim 9$.

To estimate the contribution of our sample, we calculated the volume based on the area covered by the survey and the redshifts and M_{UV} derived by BEAGLE. The luminosity function point for this sample is computed utilizing the V_{max} method (Schmidt 1968). The number density of galaxies within a specific magnitude range relies on the maximum volume, V_{max} , within which each galaxy could have been chosen. The comoving number density of sources per absolute magnitude, $\Phi(M_{UV})$, is calculated as follows:

$$\Phi(M_{UV}) \Delta M_{UV} = \sum_{i=1}^N \left(\frac{1}{V_{max,i}} \right), \quad (3)$$

where the volume for a given galaxy, i , is computed as

$$V_{max,i} = \int_{\Omega} \int_{z_{min,i}}^{z_{max,i}} \frac{dV}{d\Omega dz}, \quad (4)$$

with $z_{min,i}$ and $z_{max,i}$ here defined as the 95% confidence interval for the redshift derived with BEAGLE. The associated Poissonian uncertainties are given for the UV luminosity function by

$$\sigma_{\phi}(M_{UV}) \Delta M_{UV} = \sqrt{\frac{1}{N} \sum_{i=1}^N \frac{1}{V_{max,i}^2}}, \quad (5)$$

where N is the number of galaxies within the UV magnitude range.

We accounted for both completeness and contamination. To achieve this, we utilized a semi-empirical simulation: the Deep Realistic Extragalactic Model (DREaM; Drakos et al. 2022). This simulation provides a realistic distribution of the flux, size,

morphology, and redshift of galaxies from $z \sim 0$ –13. Using this galaxy catalog, we generated realistic raw NIRCcam data with the Multi-Instrument Ramp Generator (Hilbert et al. 2019) for the full COSMOS-Web area. These raw images were subsequently reduced in the same manner as the COSMOS-Web images. The DREaM catalog adapted for COSMOS-Web will be presented in detail in N. Drakos et al. (2024, in preparation). From these simulations, we performed the same analysis (e.g., flux extraction, SED fitting, selection criteria) as that conducted on the actual data to estimate the completeness and contamination of our sample. These factors were then incorporated into the calculation of volume density of $z > 9$ galaxies in the first epoch of COSMOS-Web.

In Figure 10, we present a compilation of several studies at $z \sim 9$ from McLure et al. (2013), Oesch et al. (2013), Bouwens et al. (2013, 2015), Finkelstein et al. (2015), Finkelstein (2016), McLeod et al. (2016), Stefanon et al. (2019), Bowler et al. (2020), Bouwens et al. (2021), Kauffmann et al. (2022), Naidu et al. (2022), Donnan et al. (2023b), Harikane et al. (2022), and Pérez-González et al. (2023), as well as the best-fitting Schechter functions from Bouwens et al. (2015) and Bowler et al. (2020) and the double power-law function from Harikane et al. (2024). At the mean redshift of our sample ($z = 10.0$), we measure a volume density of $(7.26^{+4.85}_{-3.85}) \times 10^{-5} \text{ Mpc}^{-3}$ per magnitude at $M_{UV} = -20.19^{+0.9}_{-1.1}$. This is about a factor of ~ 3 times above expectation from the $z \sim 10$ functional form of the UVLF derived by Harikane et al. (2024) but well aligned with some other works that find a relative excess of $z > 10$ candidates (Finkelstein et al. 2023). We also compared our results with predictions from the hydrodynamic simulations of galaxy formation and evolution FLARES (Lovell et al. 2021; Vijayan et al. 2021) and the UNIVERSEMACHINE (Behroozi et al. 2019) simulations at $z \sim 10$. Our results are in very good agreement with these simulations. As discussed previously in Section 4.2.3, despite this relative excess of UV-bright systems,

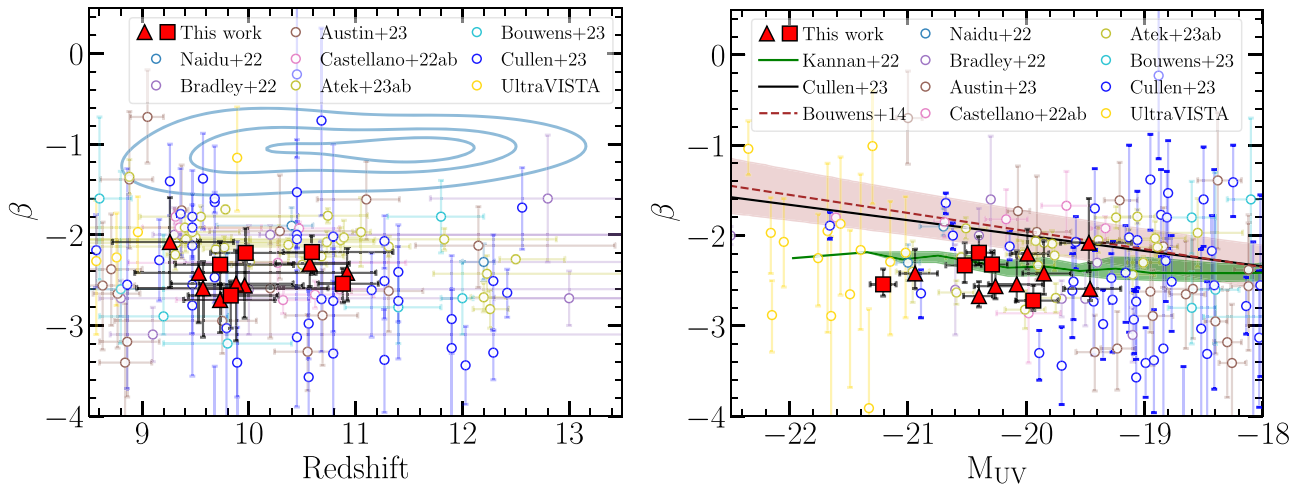


Figure 5. Left: ultraviolet spectral slope (β) as a function of redshift for our $z \geq 9$ sample (red points) and a compilation of galaxies detected by JWST at $z > 8.5$. In addition, we included an extra sample of bright high-redshift galaxies (yellow points) obtained from wide-area, ground-based near-IR imaging within the COSMOS/ UltraVISTA field (at $z \sim 8$ –10) from Donnan et al. (2023b). The blue contours represent the parameter space occupied by a synthetic sample of galaxies at $5 > z > 6$, for which their broad emission lines in optical spectra could be important contaminants in F150W dropouts at $z \geq 9$ (McKinney et al. 2023). The clear separation of our galaxies from this region provides further support for the accuracy of our redshift measurements. Right: β as a function of M_{UV} . The best fits from Cullen et al. (2023, for $8 < z < 16$ galaxies) and Bouwens et al. (2014, for $z \sim 7$ galaxies) and the prediction from the THESAN simulations (for $z \sim 9$ galaxies; Kannan et al. 2022) are displayed in black, brown, and green, respectively. Our galaxies are slightly bluer than the trends presented in Bouwens et al. (2014) and Cullen et al. (2023), but they are closely related to the trend from Kannan et al. (2022). For each of the two panels, results for our $z \geq 9$ galaxy sample are displayed in red and put into perspective with a compilation of recent results from the JWST at $z > 8.5$. The difference between red squares and red triangles is the same as in Figure 3.

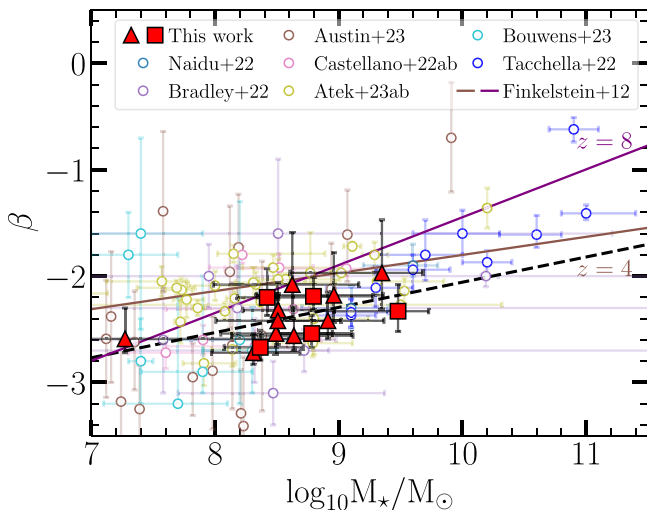


Figure 6. Ultraviolet spectral slope (β) as a function of the stellar mass of our $z \geq 9$ sample (red points) and a compilation of galaxies detected by JWST at $z > 8.5$. In addition, we included an extra sample of bright ($H < 26.6$) high-redshift galaxies ($z = 8.5$ –11) selected by Finkelstein et al. (2012) in the CANDELS fields (Grogin et al. 2011; Koekemoer et al. 2011) and studied in Tacchella et al. (2022). We also added the trend between β and stellar mass at $z = 4$ and $z = 8$ derived by Finkelstein et al. (2012, brown and purple lines, respectively). While β does not show a significant correlation with redshift or absolute UV magnitude, we observe a clear correlation between β and stellar mass for our sample, with a slope of 0.24 ± 0.10 (dashed line).

none of these galaxies exceed allowable expectations for galaxy formation at these redshifts within a Λ CDM framework.

6. Discussion

Interestingly, early JWST measurements of the UVLF show an abundance of galaxies which is evolving more shallowly downward with increasing redshift than predicted by simulations (e.g., Harikane et al. 2022, 2024; Finkelstein et al. 2023). This result may indicate that at $z \geq 9$ the global star formation

efficiency (i.e., the fraction of baryons in a halo converted into stars) may be higher than at lower redshifts, or/and the stellar IMF may be top-heavy. Either of these would result in galaxies being more UV luminous than predicted, leading to the observed excess. Both of these may be expected in the first 500 Myr of cosmic time at $z \geq 9$, when the physical conditions present in star-forming regions are vastly different from today. COSMOS-Web provides access to a specific range of parameters for the EoR that cannot be explored by smaller surveys focusing on only the brightest galaxies (with $M_{UV} \leq -20$), as noted by Casey et al. (2023) and Finkelstein et al. (2023). This parameter space is crucial for determining the upper limit of the UV luminosity function and identifying any potential overabundance of bright galaxies during the EoR. This study will be conducted in detail in a future paper and is outside the scope of this paper.

The anticipated count of galaxies at $z \geq 9$ in COSMOS-Web, derived through a direct calculation based on the gathered UV luminosity functions, is 8–10 (Casey et al. 2023). As such, we have detected 50% more sources than the upper limit of these predictions. This is intriguing and may have several causes. In contrast to pre-JWST studies, we benefit from unprecedented near-IR resolution and sensitivity at $\lambda > 1.6 \mu\text{m}$. In particular, in this study, the detection of very-high-redshift sources is made possible by the long-wavelength filters, F277W and F444W. It could also be caused by the cosmic variance. Star formation in the $z > 7$ Universe is expected to be highly clustered, with $\sim 40\%$ – 50% of the SFR density concentrated in the progenitors of massive galaxy clusters (e.g., Chiang et al. 2017).

This could come from an excess of bright galaxies and an underestimation of the bright end of the luminosity function. This excess of bright galaxies starts to be visible for galaxies both very bright ($M_{UV} \sim -22$) detected with HST (e.g., Bagley et al. 2024), in contrast to the predicted smooth evolution of a Schechter function from lower redshifts. This excess of galaxies is also observed with JWST at lower UV absolute

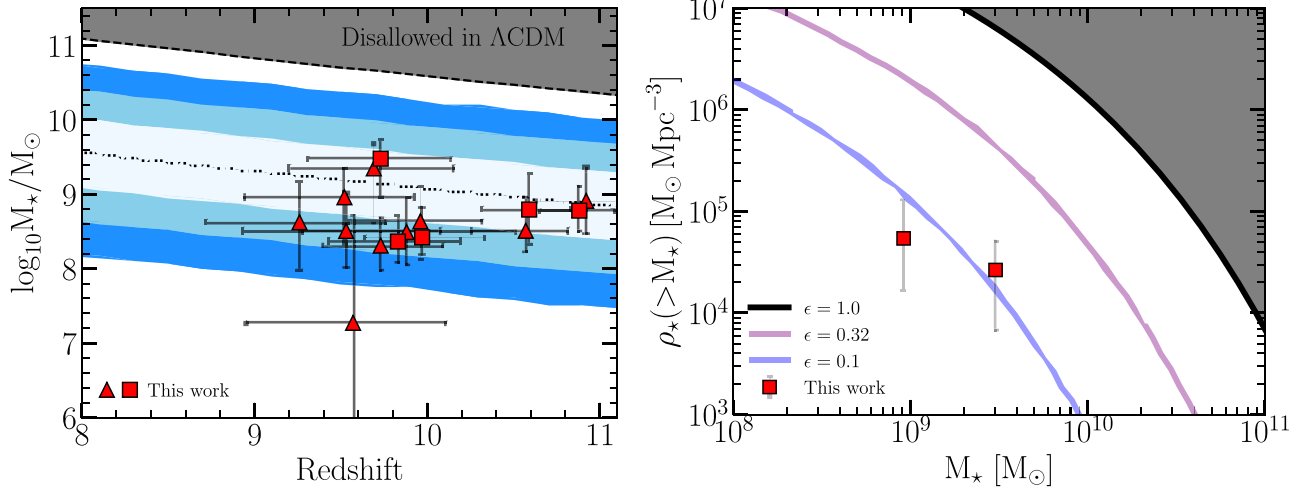


Figure 7. Left: stellar mass as a function of redshift for our $z \geq 9$ sample (red points). The PDF of the most massive galaxy predicted by EVS from Lovell et al. (2023) is also displayed in shades of blue (1, 2, and 3σ) around the median value of the expected maximum stellar mass for the volume of this survey. The dashed line shows the 3σ upper limit assuming a stellar fraction of unity. The absence of galaxies more than 1σ above this limit indicates no tension between our observations and the Λ CDM cosmology. Right: the comoving stellar mass density within galaxies that are more massive than M_* (for two stellar mass bins) at the median redshift of our sample can be expressed for three different assumed values of the conversion efficiency (ϵ), which represents the transformation of a halo’s cosmic allotment of baryons into stars. The stellar masses derived in our sample do not present any tension with standard Λ CDM models. This implies a conversion efficiency ~ 0.1 . This plot has been done using the code available in Boylan-Kolchin (2023). The difference between red squares and red triangles is the same as in Figure 3.

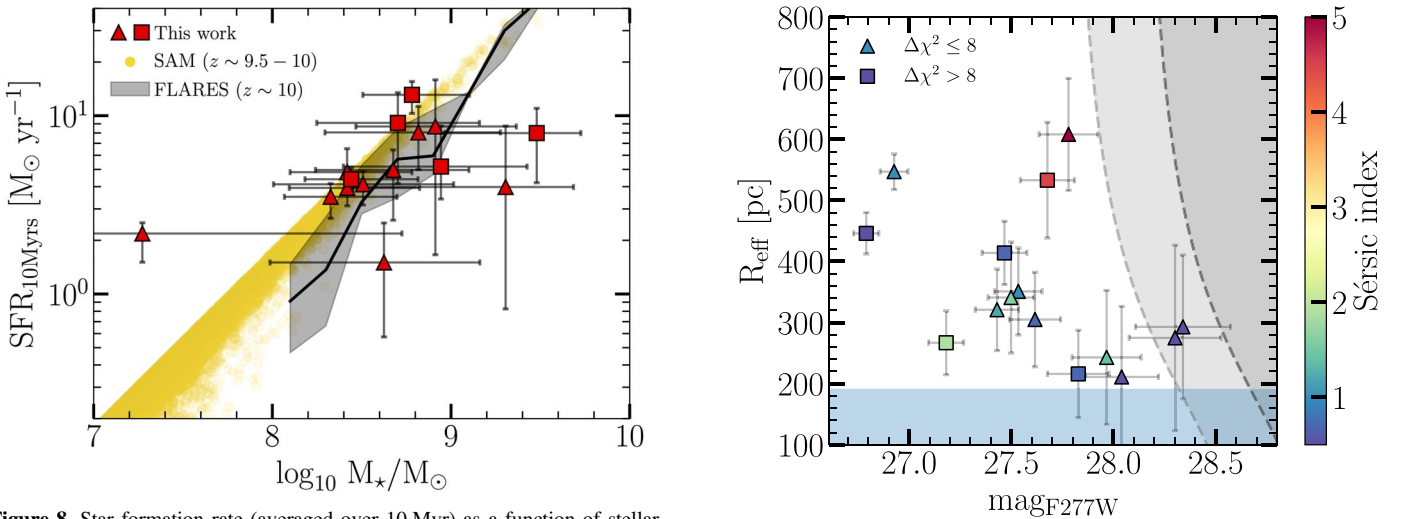


Figure 8. Star formation rate (averaged over 10 Myr) as a function of stellar mass for our $z \geq 9$ sample (red points). The expected values from the hydrodynamic simulation FLARES (Lovell et al. 2021; Vijayan et al. 2021) at $z \sim 10$ and Santa Cruz semi-empirical simulation (SAM; e.g., Yung et al. 2019) for galaxies at $z = 9.5\text{--}10$ are displayed in black and yellow, respectively. The difference between red squares and red triangles is the same as in Figure 3.

magnitudes ($M_{\text{UV}} \sim -19 - -20$; e.g., Finkelstein et al. 2023). A last possibility would be a contamination by low-redshift galaxies. However, in view of the arguments presented in Section 4.2.1, we consider that this is not the hypothesis to be favored here. We will explore these possibilities in detail in a future paper. We would point out, however, that we have not taken into account the effects of completeness and contamination in calculating the UVLF. This will be the subject of a future paper. This would tend to qualify our point as a lower limit in the UVLF rather than a measurement.

Recent studies have evoked the hypothesis that galaxies detected by the JWST for an area half the size as the area covered by the first part of the COSMOS-Web survey could have masses so high that they were difficult to realize in a

Figure 9. Effective radius as a function of F277W magnitude for our $z \geq 9$ sample measured by SE++, color-coded according to the Sérsic index. The blue shaded region represents the effective radius of the F277W JWST PSF ($0.092''$) at the average redshift of our sample ($z_{\text{mean,beagle}} = 9.98$). The detected galaxies are compact. While the faintest galaxies are consistent with unresolved sizes, the brightest galaxies are clearly resolved. The gray shaded regions represent the detectability limits (5σ in F277W) for resolved sources at depths corresponding to two and four NIRCcam exposures.

standard Λ CDM cosmology (e.g., Labbé et al. 2023) at $7.4 < z < 9.1$. The galaxies presented in this study have a much lower stellar mass, with stellar masses derived with the Dense-Basis SED-fitting code ranging between $1.8 \times 10^7 M_\odot$ and $3.0 \times 10^9 M_\odot$. Stellar mass values using different SFHs and different SED-fitting codes are consistent with these results. We have compared these masses with the method of EVS derived by Lovell et al. (2023) and adapted to the solid angle of this survey. It would have been necessary to detect galaxies about ~ 50 times more massive (assuming a baryon-to-stellar conversion rate of 1) to enter a parameter space disallowed by Λ CDM for the most massive galaxies. We have

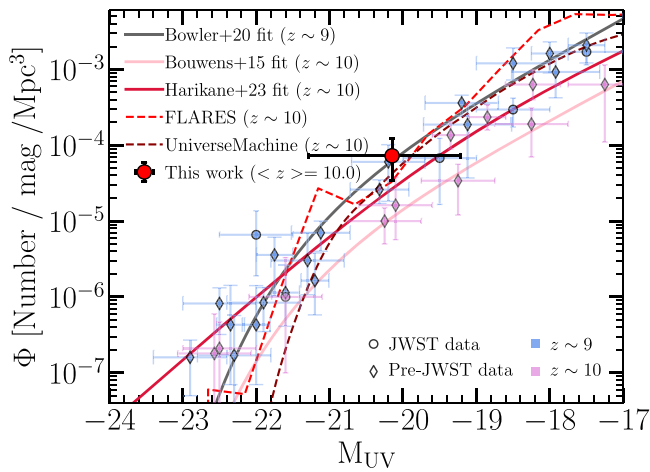


Figure 10. Rest-frame UVLF at $z \sim 9$ – 10 . We include data from the literature from McLure et al. (2013), Oesch et al. (2013), Bouwens et al. (2013, 2015), Finkelstein et al. (2015), Finkelstein (2016), McLeod et al. (2016), Stefanon et al. (2019), Bowler et al. (2020), Bouwens et al. (2021), Kauffmann et al. (2022), Naidu et al. (2022), Donnan et al. (2023b), Harikane et al. (2022), and Pérez-González et al. (2023) at $z \sim 9$ and at $z \sim 10$ (gray-blue and pink points respectively). The best-fitting Schechter functions at $z \sim 9$ from Bowler et al. (2020) and from Bouwens et al. (2015) at $z \sim 10$ are shown with the gray and red solid lines, respectively. The double power-law fit at $z \sim 10$ from Harikane et al. (2024) is also displayed in red. We differentiate points obtained with the JWST (circles) from points obtained before its launch (diamonds). In addition, we also display predictions from the FLARES (Lovell et al. 2021; Vijayan et al. 2021) and the UNIVERSEMACHINE (Behroozi et al. 2019) simulations at $z \sim 10$.

also used the study of Boylan-Kolchin (2023) and adapted it to our case to compare the cumulative mass of our sample with the available supply of baryonic matter within dark matter haloes. We are well below the theoretical value if all available baryons had been converted into stars (i.e., with an efficiency of converting baryons into stars ϵ equal to unity) and the cumulative mass of galaxies detected in this study. For our sample, we find a value of ϵ about ~ 0.1 (see right panel of Figure 7). We do, however, note that at high redshift the stellar masses can be uncertain due to an evolution of the IMF at very high redshift, when the ISM is less rich in metals, and to the contribution of active galactic nuclei that complicates stellar mass estimates (e.g., Labbé et al. 2023).

7. Conclusions

In this paper, we report the detection of high-redshift candidates with $z > 9$ using the initial JWST release of COSMOS-Web. These observations cover 77 arcmin^2 with the four NIRCcam filters (F115W, F150W, F277W, and F444W) with an overlap with MIRI (F770W) of 8.7 arcmin^2 .

We detect 15 galaxies within the redshift range (9.3–10.9), representing a period, relatively short in duration, between 400 Myr and 500 Myr after the Big Bang, a time of rapid change in galaxy evolution.

We have used three SED-fitting codes to derive the redshifts of these galaxies (EAZY, BEAGLE, BAGPIPES). These three codes are in good agreement, with redshifts agreeing between them within their uncertainties. However, we note that BAGPIPES systematically gives slightly lower redshifts than the two other SED-fitting codes. Only spectroscopic follow-up of these sources will allow us to determine in a robust way the redshifts of these galaxies.

We divided our sample in two parts in order to separate galaxies with more robust redshifts ($\Delta\chi^2 > 8$) from those with less robust redshifts ($\Delta\chi^2 < 8$), where $\Delta\chi^2$ represents the difference between the EAZY fit without any constraints ($0 < z < 15$) and the “low”-redshift solution ($z < 7$). We did not find any significant difference for all the parameters presented in this paper between these two subsamples, which would suggest that our derivation of redshifts is robust.

Although the galaxies detected in this study all have blue UV slopes ($-2.7 < \beta < -2.0$), we did not detect any extreme values ($\beta < -3$) as has been reported recently in other studies at similar redshifts. On average, these galaxies display greater luminosities in comparison to the majority of $z \sim 9$ candidates discovered by JWST, as documented in the existing literature. Surprisingly, despite their increased brightness, these galaxies exhibit similar blue hues in their rest-frame UV colors. This observation suggests that, even at 400 Myr after the Big Bang, the star formation occurs from an ISM that is already enriched in metals.

We have derived the UV luminosity function for our sample. We measure a volume density of $(7.26_{-3.85}^{+4.85}) \times 10^{-5} \text{ Mpc}^{-3}$ per magnitude at $M_{\text{UV}} = -20.19_{-1.1}^{+0.9}$. We find an excess of bright galaxies with a detection almost 3 times the expected number of galaxies at $z \geq 9$ in the volume of this survey. We therefore find a value above the fit derived by Harikane et al. (2024) at $z \sim 10$, or Bouwens et al. (2015) prior to the commissioning of JWST for galaxies at $z \sim 10$, but well aligned with some other works that find a relative excess of $z > 10$ candidates (e.g., Finkelstein et al. 2023; McLeod et al. 2024; Adams et al. 2024; Donnan et al. 2023a, 2023b) as well as with predictions from simulations, e.g., FLARES (Lovell et al. 2021; Vijayan et al. 2021) or UNIVERSEMACHINE (Behroozi et al. 2019).

We have derived the stellar masses of our sample, which are between $1.8 \times 10^7 M_{\odot}$ and $3.0 \times 10^9 M_{\odot}$. Comparing these results to the maximum expected mass according to ΛCDM (Lovell et al. 2023; Boylan-Kolchin 2023), we find no tension between observations and theory.

This study focuses on the first observations of the COSMOS-Web survey and represents only 4% of the total survey area. When the entire survey is completed, the statistics and results given by this study will be refined, the cosmic variance reduced to its minimum, and the statistics will be sufficient to have robust constraints on the bright end of the UVLF during the EoR. These results will be complementary with other deeper but smaller JWST surveys probing different regions of parameter space.

Acknowledgments

We thank Sandro Tacchella and the NIRCcam team for sharing the wisps templates. We acknowledge that the location where most of this work took place, the University of Texas at Austin, sits on the Indigenous lands of Turtle Island, the ancestral name for what now is called North America. Moreover, we would like to acknowledge the Alabama-Coushatta, Caddo, Carrizo/Comecrudo, Coahuiltecan, Comanche, Kickapoo, Lipan Apache, Tonkawa and Ysleta Del Sur Pueblo, and all the American Indian and Indigenous Peoples and communities who have been or have become a part of these lands and territories in Texas. M.F. thanks Gene Leung for helpful discussions. M.F. acknowledges support from NSF grant AST-2009577 and NASA JWST GO program 1727. Support for this work was provided by NASA through grant

Nos. JWST-GO-01727 and HST-AR-15802 awarded by the Space Telescope Science Institute, which is operated by the Association of Universities for Research in Astronomy, Inc., under NASA contract NAS 5-26555. C.M.C. thanks the National Science Foundation for support through grants AST-1814034 and AST-2009577 as well as the University of Texas at Austin College of Natural Sciences for support; C.M.C. also acknowledges support from the Research Corporation for Science Advancement from a 2019 Cottrell Scholar Award sponsored by IF/THEN, an initiative of Lyda Hill Philanthropies. The French part of the COSMOS team is partly supported by the Centre National d'Etudes Spatiales (CNES). O.I. acknowledges the funding of the French Agence Nationale de la Recherche for the project iMAGE (grant No. ANR-22-CE31-0007). This work was made possible by utilizing the

CANDIDE cluster at the Institut d'Astrophysique de Paris, which was funded through grants from the PNCG, CNES, DIM-ACAV, and the Cosmic Dawn Center and is maintained by S. Rouberol. Some data presented in this paper were obtained from the Mikulski Archive for Space Telescopes (MAST) at the Space Telescope Science Institute. The specific observations analyzed can be accessed via DOI:[10.17909/ahsg-ek22](https://doi.org/10.17909/ahsg-ek22).

Appendix Cutouts of the $z \geq 9$ Sample

In this appendix, we provide postage-stamp (HST/F814W, JWST/F115W, JWST/F150W, JWST/F277W, JWST/F444W, and MIRI/F770W when available) images of the 15 $z > 9$ candidates listed in Figure A1.

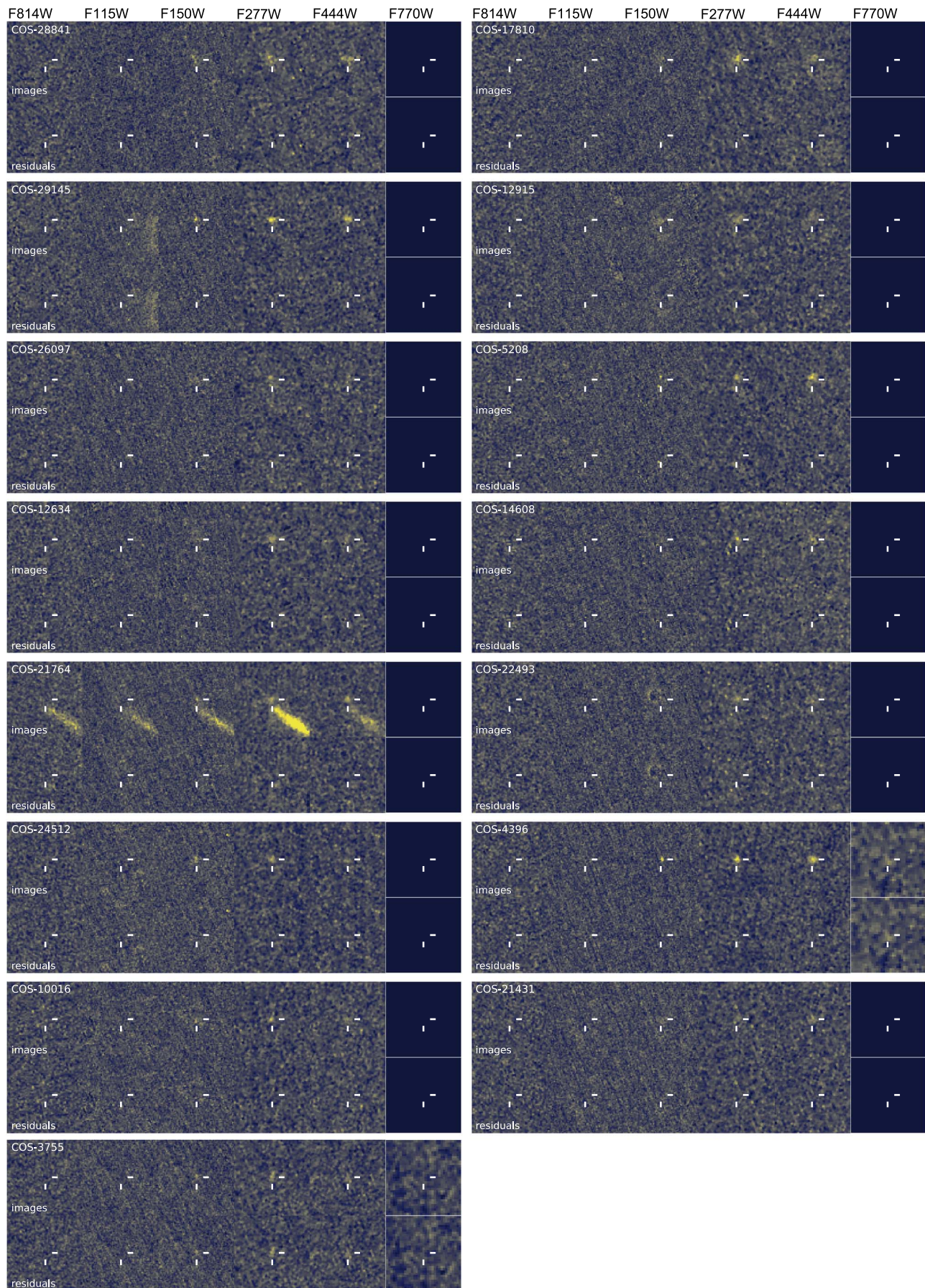


Figure A1. For each galaxy, we show a $2''$ stamp image centered on our detections on the upper line and the residuals on the lower line after subtraction of the galaxy models found by SE++ for the four NIRCcam filters, the MIRI filter, and the HST/F814W filter. Black squares for MIRI indicate that the galaxy is out of the MIRI coverage.

ORCID iDs

Maximilien Franco  <https://orcid.org/0000-0002-3560-8599>
 Hollis B. Akins  <https://orcid.org/0000-0003-3596-8794>
 Caitlin M. Casey  <https://orcid.org/0000-0002-0930-6466>
 Steven L. Finkelstein  <https://orcid.org/0000-0001-8519-1130>
 Marko Shuntov  <https://orcid.org/0000-0002-7087-0701>
 Katherine Chworowsky  <https://orcid.org/0000-0003-4922-0613>
 Andreas L. Faisst  <https://orcid.org/0000-0002-9382-9832>
 Seiji Fujimoto  <https://orcid.org/0000-0001-7201-5066>
 Olivier Ilbert  <https://orcid.org/0000-0002-7303-4397>
 Anton M. Koekemoer  <https://orcid.org/0000-0002-6610-2048>
 Daizhong Liu  <https://orcid.org/0000-0001-9773-7479>
 Christopher C. Lovell  <https://orcid.org/0000-0001-7964-5933>
 Claudia Maraston  <https://orcid.org/0000-0001-7711-3677>
 Henry Joy McCracken  <https://orcid.org/0000-0002-9489-7765>
 Jed McKinney  <https://orcid.org/0000-0002-6149-8178>
 Brant E. Robertson  <https://orcid.org/0000-0002-4271-0364>
 Micaela B. Bagley  <https://orcid.org/0000-0002-9921-9218>
 Jaclyn B. Champagne  <https://orcid.org/0000-0002-6184-9097>
 Olivia R. Cooper  <https://orcid.org/0000-0003-3881-1397>
 Xuheng Ding  <https://orcid.org/0000-0001-8917-2148>
 Nicole E. Drakos  <https://orcid.org/0000-0003-4761-2197>
 Andrea Enia  <https://orcid.org/0000-0002-0200-2857>
 Steven Gillman  <https://orcid.org/0000-0001-9885-4589>
 Ghassem Gozaliasl  <https://orcid.org/0000-0002-0236-919X>
 Santosh Harish  <https://orcid.org/0000-0003-0129-2079>
 Christopher C. Hayward  <https://orcid.org/0000-0003-4073-3236>
 Michaela Hirschmann  <https://orcid.org/0000-0002-3301-3321>
 Shuowen Jin  <https://orcid.org/0000-0002-8412-7951>
 Jeyhan S. Kartaltepe  <https://orcid.org/0000-0001-9187-3605>
 Vasily Kokorev  <https://orcid.org/0000-0002-5588-9156>
 Clotilde Laigle  <https://orcid.org/0009-0008-5926-818X>
 Arianna S. Long  <https://orcid.org/0000-0002-7530-8857>
 Georgios Magdis  <https://orcid.org/0000-0002-4872-2294>
 Guillaume Mahler  <https://orcid.org/0000-0003-3266-2001>
 Crystal L. Martin  <https://orcid.org/0000-0001-9189-7818>
 Richard Massey  <https://orcid.org/0000-0002-6085-3780>
 Bahram Mobasher  <https://orcid.org/0000-0001-5846-4404>
 Louise Paquereau  <https://orcid.org/0000-0003-2397-0360>
 Alvio Renzini  <https://orcid.org/0000-0002-7093-7355>
 Jason Rhodes  <https://orcid.org/0000-0002-4485-8549>
 R. Michael Rich  <https://orcid.org/0000-0003-0427-8387>
 Kartik Sheth  <https://orcid.org/0000-0002-5496-4118>
 John D. Silverman  <https://orcid.org/0000-0002-0000-6977>
 Martin Sparre  <https://orcid.org/0000-0002-9735-3851>
 Margherita Talia  <https://orcid.org/0000-0003-4352-2063>
 Benny Trakhtenbrot  <https://orcid.org/0000-0002-3683-7297>
 Francesco Valentino  <https://orcid.org/0000-0001-6477-4011>
 Aswin P. Vijayan  <https://orcid.org/0000-0002-1905-4194>
 Stephen M. Wilkins  <https://orcid.org/0000-0003-3903-6935>
 Lilan Yang  <https://orcid.org/0000-0002-8434-880X>
 Jorge A. Zavala  <https://orcid.org/0000-0002-7051-1100>

References

Adams, N. J., Conselice, C. J., Austin, D., et al. 2024, *ApJ*, 965, 169
 Adams, N. J., Conselice, C. J., Ferreira, L., et al. 2023, *MNRAS*, 518, 4755
 Aihara, H., Aisayad, Y., Ando, M., et al. 2022, *PASJ*, 74, 247

Arrabal Haro, P., Dickinson, M., Finkelstein, S. L., et al. 2023a, *Natur*, 622, 707
 Arrabal Haro, P., Dickinson, M., Finkelstein, S. L., et al. 2023b, *ApJL*, 951, L22
 Atek, H., Chemerynska, I., Wang, B., et al. 2023b, *MNRAS*, 524, 5486
 Atek, H., Shuntov, M., Furtak, L. J., et al. 2023a, *MNRAS*, 519, 1201
 Austin, D., Adams, N. J., Conselice, C. J., et al. 2023, *ApJL*, 952, L7
 Bagley, M. B., Finkelstein, S. L., Rojas-Ruiz, S., et al. 2024, *ApJ*, 961, 209
 Behroozi, P., Wechsler, R. H., Hearin, A. P., & Conroy, C. 2019, *MNRAS*, 488, 3143
 Beichman, C. A., Rieke, M., Eisenstein, D., et al. 2012, *Proc. SPIE*, 8442, 84422N
 Bertin, E., & Arnouts, S. 1996, *A&AS*, 117, 393
 Bertin, E., Schefer, M., Apostolakis, N., et al. 2020, in ASP Conf. Ser. 527, *Astronomical Data Analysis Software and Systems XXIX*, ed. R. Pizzo et al. (San Francisco, CA: ASP), 461
 Bezanson, R., Labbe, I., Whitaker, K. E., et al. 2022, arXiv:2212.04026
 Bouwens, R., Illingworth, G., Oesch, P., et al. 2023, *MNRAS*, 523, 1009
 Bouwens, R. J., Oesch, P. A., Illingworth, G. D., et al. 2013, *ApJL*, 765, L16
 Bouwens, R. J., Oesch, P. A., Stefanon, M., et al. 2021, *AJ*, 162, 47
 Bouwens, R. J., Illingworth, G. D., Oesch, P. A., et al. 2014, *ApJ*, 793, 115
 Bouwens, R. J., Illingworth, G. D., Oesch, P. A., et al. 2015, *ApJ*, 803, 34
 Bowler, R. A. A., Jarvis, M. J., Dunlop, J. S., et al. 2020, *MNRAS*, 493, 2059
 Boyett, K., Trenti, M., Leethochawalit, N., et al. 2024, *NatAs*, 8, 657
 Boylan-Kolchin, M. 2023, *NatAs*, 7, 731
 Bradley, L. D., Coe, D., Brammer, G., et al. 2023, *ApJ*, 955, 13
 Brammer, G. B., van Dokkum, P. G., & Coppi, P. 2008, *ApJ*, 686, 1503
 Bruzual, G., & Charlot, S. 2003, *MNRAS*, 344, 1000
 Bunker, A. J., Saxena, A., Cameron, A. J., et al. 2023, *A&A*, 677, A88
 Bushouse, H., Eisenhamer, J., Dencheva, N., et al. 2023, JWST Calibration Pipeline v1.9.6, Zenodo, doi:10.5281/zenodo.7714020
 Calzetti, D., Armus, L., Bohlin, R. C., et al. 2000, *ApJ*, 533, 682
 Calzetti, D., Kinney, A. L., & Storchi-Bergmann, T. 1994, *ApJ*, 429, 582
 Cameron, A. J., Saxena, A., Bunker, A. J., et al. 2023, *A&A*, 677, A115
 Capak, P., Aussel, H., Ajiki, M., et al. 2007, *ApJS*, 172, 99
 Carnall, A. C., McLure, R. J., Dunlop, J. S., & Davé, R. 2018, *MNRAS*, 480, 4379
 Casey, C. M., Akins, H. B., Shuntov, M., et al. 2024, *ApJ*, 965, 98
 Casey, C. M., Kartaltepe, J. S., Drakos, N. E., et al. 2023, *ApJ*, 954, 31
 Casey, C. M., Narayanan, D., & Cooray, A. 2014, *PhR*, 541, 45
 Castellano, M., Fontana, A., Treu, T., et al. 2022, *ApJL*, 938, L15
 Castellano, M., Fontana, A., Treu, T., et al. 2023, *ApJL*, 948, L14
 Chabrier, G. 2003, *PASP*, 115, 763
 Chevillard, J., & Charlot, S. 2016, *MNRAS*, 462, 1415
 Chiang, Y.-K., Overzier, R. A., Gebhardt, K., & Henriques, B. 2017, *ApJL*, 844, L23
 Condon, J. J. 1997, *PASP*, 109, 166
 Conroy, C., & Gunn, J. E. 2010, FSPS: Flexible Stellar Population Synthesis, *Astrophysics Source Code Library*, ascl:1010.043
 Cullen, F., McLure, R. J., McLeod, D. J., et al. 2023, *MNRAS*, 520, 14
 Curtis-Lake, E., Carniani, S., Cameron, A., et al. 2023, *NatAs*, 7, 622
 Donnan, C. T., McLeod, D. J., Dunlop, J. S., et al. 2023b, *MNRAS*, 518, 6011
 Donnan, C. T., McLeod, D. J., McLure, R. J., et al. 2023a, *MNRAS*, 520, 4554
 Drakos, N. E., Villaseñor, B., Robertson, B. E., et al. 2022, *ApJ*, 926, 194
 Dunlop, J. S., Rogers, A. B., McLure, R. J., et al. 2013, *MNRAS*, 432, 3520
 Eisenstein, D. J., Willott, C., Alberts, S., et al. 2023, arXiv:2306.02465
 Eldridge, J. J., & Stanway, E. R. 2009, *MNRAS*, 400, 1019
 Ferland, G. J., Chatzikos, M., Guzmán, F., et al. 2017, *RMxAA*, 53, 385
 Finkelstein, S. L. 2016, *PASA*, 33, e037
 Finkelstein, S. L., Bagley, M. B., Ferguson, H. C., et al. 2023, *ApJL*, 946, L13
 Finkelstein, S. L., Bagley, M. B., Haro, P. A., et al. 2022, *ApJL*, 940, L55
 Finkelstein, S. L., Papovich, C., Salmon, B., et al. 2012, *ApJ*, 756, 164
 Finkelstein, S. L., Ryan, R. E. J., Papovich, C., et al. 2015, *ApJ*, 810, 71
 Fujimoto, S., Haro, P. A., Dickinson, M., et al. 2023, *ApJL*, 949, L25
 Gaia Collaboration, Brown, A. G. A., Vallenari, A., et al. 2021, *A&A*, 649, A1
 Garaldi, E., Kannan, R., Smith, A., et al. 2022, *MNRAS*, 512, 4909
 Grogan, N. A., Kocovski, D. D., Faber, S. M., et al. 2011, *ApJS*, 197, 35
 Gumbel, E. J. 1958, *Statistics of Extremes* (New York: Columbia Univ. Press)
 Gutkin, J., Charlot, S., & Bruzual, G. 2016, *MNRAS*, 462, 1757
 Hainline, K. N., Johnson, B. D., Robertson, B., et al. 2024, *ApJ*, 964, 71
 Harikane, Y., Inoue, A. K., Mawatari, K., et al. 2022, *ApJ*, 929, 1
 Harikane, Y., Nakajima, K., Ouchi, M., et al. 2024, *ApJ*, 960, 56
 Harikane, Y., Ouchi, M., Oguri, M., et al. 2023, *ApJS*, 265, 5
 Harrison, I., & Coles, P. 2011, *MNRAS*, 418, L20
 Hilbert, B., Sahlmann, J., Volk, K., et al. 2019, spacetelescope/mirage: First github release v1.1.1, Zenodo, doi:10.5281/zenodo.3519262

- Hutter, A., Dayal, P., Yepes, G., et al. 2021, *MNRAS*, 503, 3698
- Iyer, K., & Gawiser, E. 2017, *ApJ*, 838, 127
- Iyer, K. G., Gawiser, E., Faber, S. M., et al. 2019, *ApJ*, 879, 116
- Kannan, R., Garaldi, E., Smith, A., et al. 2021, *MNRAS*, 511, 4005
- Kannan, R., Smith, A., Garaldi, E., et al. 2022, *MNRAS*, 514, 3857
- Kauffmann, O. B., Ilbert, O., Weaver, J. R., et al. 2022, *A&A*, 667, A65
- Koekemoer, A. M., Aussel, H., Calzetti, D., et al. 2007, *ApJS*, 172, 196
- Koekemoer, A. M., Faber, S. M., Ferguson, H. C., et al. 2011, *ApJS*, 197, 36
- Kotz, S., & Nadarajah, S. 2000, *Extreme Value Distributions* (Singapore: World Scientific)
- Kümmel, M., Bertin, E., Schefer, M., et al. 2020, in ASP Conf. Ser. 527, *Astronomical Data Analysis Software and Systems XXIX*, ed. R. Pizzo et al., 29
- Labbé, I., van Dokkum, P., Nelson, E., et al. 2023, *Natur*, 616, 266
- Larson, R. L., Finkelstein, S. L., Kocevski, D. D., et al. 2023, *ApJL*, 953, L29
- Larson, R. L., Hutchison, T. A., Bagley, M., et al. 2023, *ApJ*, 958, 141
- Leung, G. C. K., Bagley, M. B., Finkelstein, S. L., et al. 2023, *ApJL*, 954, L46
- Liu, D., Lang, P., Magnelli, B., et al. 2019, *ApJS*, 244, 40
- Lovell, C. C., Harrison, I., Harikane, Y., Tacchella, S., & Wilkins, S. M. 2023, *MNRAS*, 518, 2511
- Lovell, C. C., Vijayan, A. P., Thomas, P. A., et al. 2021, *MNRAS*, 500, 2127
- Marshall, M. A., Wilkins, S., Di Matteo, T., et al. 2022, *MNRAS*, 511, 5475
- Mason, C. A., Trenti, M., & Treu, T. 2023, *MNRAS*, 521, 497
- McCracken, H. J., Milvang-Jensen, B., Dunlop, J., et al. 2012, *A&A*, 544, A156
- McKinney, J., Finnerty, L., Casey, C. M., et al. 2023, *ApJL*, 946, L39
- McLeod, D. J., Donnan, C. T., McLure, R. J., et al. 2024, *MNRAS*, 527, 5004
- McLeod, D. J., McLure, R. J., & Dunlop, J. S. 2016, *MNRAS*, 459, 3812
- McLure, R. J., Dunlop, J. S., Bowler, R. A. A., et al. 2013, *MNRAS*, 432, 2696
- Meurer, G. R., Heckman, T. M., & Calzetti, D. 1999, *ApJ*, 521, 64
- Naidu, R. P., Oesch, P. A., van Dokkum, P., et al. 2022, *ApJL*, 940, L14
- Oesch, P. A., Bouwens, R. J., Illingworth, G. D., et al. 2013, *ApJ*, 773, 75
- Oesch, P. A., Brammer, G., van Dokkum, P. G., et al. 2016, *ApJ*, 819, 129
- Oke, J. B., & Gunn, J. E. 1983, *ApJ*, 266, 713
- Pérez-González, P. G., Barro, G., Annunziatella, M., et al. 2023, *ApJL*, 946, L16
- Perrin, M. D., Sivaramakrishnan, A., Lajoie, C.-P., et al. 2014, *Proc. SPIE*, 9143, 91433X
- Planck Collaboration, Aghanim, N., Akrami, Y., et al. 2020, *A&A*, 641, A6
- Pontoppidan, K. M., Barrientes, J., Blome, C., et al. 2022, *ApJL*, 936, L14
- Rieke, M. J., Baum, S. A., Beichman, C. A., et al. 2003, *Proc. SPIE*, 4850, 478
- Rieke, M. J., Kelly, D., & Horner, S. 2005, *Proc. SPIE*, 5904, 1
- Rieke, M. J., Kelly, D. M., Misselt, K., et al. 2023, *PASP*, 135, 028001
- Roberts-Borsani, G., Treu, T., Chen, W., et al. 2023, *Natur*, 618, 480
- Robertson, B. E., Tacchella, S., Johnson, B. D., et al. 2023, *NatAs*, 7, 611
- Schmidt, M. 1968, *ApJ*, 151, 393
- Scoville, N., Aussel, H., Brusa, M., et al. 2007, *ApJS*, 172, 1
- Smith, A., Kannan, R., Garaldi, E., et al. 2022, *MNRAS*, 512, 3243
- Smolčić, V., Novak, M., Bondi, M., et al. 2017, *A&A*, 602, A1
- Stanway, E. R., Bunker, A. J., & McMahon, R. G. 2003, *MNRAS*, 342, 439
- Stefanon, M., Labbé, I., Bouwens, R. J., et al. 2019, *ApJ*, 883, 99
- Tacchella, S., Finkelstein, S. L., Bagley, M., et al. 2022, *ApJ*, 927, 170
- Takeuchi, T. T., Yuan, F.-T., Ikeyama, A., Murata, K. L., & Inoue, A. K. 2012, *ApJ*, 755, 144
- Tang, M., Stark, D. P., Chen, Z., et al. 2023, *MNRAS*, 526, 1657
- Topping, M. W., Stark, D. P., Endsley, R., et al. 2022, *ApJ*, 941, 153
- Trenti, M., & Stiavelli, M. 2008, *ApJ*, 676, 767
- Treu, T., Roberts-Borsani, G., Bradac, M., et al. 2022, *ApJ*, 935, 110
- Vijayan, A. P., Lovell, C. C., Wilkins, S. M., et al. 2021, *MNRAS*, 501, 3289
- Weaver, J. R., Kauffmann, O. B., Ilbert, O., et al. 2022, *ApJS*, 258, 11
- Whitler, L., Endsley, R., Stark, D. P., et al. 2023, *MNRAS*, 519, 157
- Williams, H., Kelly, P. L., Chen, W., et al. 2023, *Sci*, 380, 416
- Yang, L., Morishita, T., Leethochawalit, N., et al. 2022, *ApJL*, 938, L17
- Yung, L. Y. A., Somerville, R. S., Finkelstein, S. L., Popping, G., & Davé, R. 2019, *MNRAS*, 483, 2983
- Yung, L. Y. A., Somerville, R. S., Finkelstein, S. L., Wilkins, S. M., & Gardner, J. P. 2024, *MNRAS*, 527, 5929
- Zavala, J. A., Buat, V., Casey, C. M., et al. 2023, *ApJL*, 943, L9